PRE-PRINT

Influence of zones of pre-existing crustal weakness on strain localization and partitioning during rifting: Insights from analogue modeling using high resolution 3D digital image correlation

Edoseghe E. Osagiede[1,2,*], Matthias Rosenau[3], Atle Rotevatn[1], Rob Gawthorpe[1], Christopher A-L. Jackson[4], and Michael Rudolf[3]

[1]Geodynamics and Basin Studies Group, Department of Earth Science, University of Bergen, Allégaten 41, 5007, Bergen, Norway.

[2]Department of Geology, University of Benin, PMB 1154, Benin City, Nigeria.

[3]Lithosphere Dynamics, Helmholtz Centre Potsdam, German Research Centre for Geosciences (GFZ), Telegraphenberg, D-14473 Potsdam, Germany.

[4]Basins Group, Department of Earth and Environmental Sciences, The University of Manchester, Williamson Building, Oxford Road, Manchester, M13 9PL, United Kingdom.

Corresponding author: Edoseghe Edwin Osagiede (edoseghe.osagiede@uib.no; edoseghe.osagiede@uniben.edu)

This manuscript has been submitted to TECTONICS. Please note that the manuscript has not undergone peer review yet. Subsequent versions of this manuscript may have slightly different content.

Influence of zones of pre-existing crustal weakness on strain localization and partitioning during rifting: Insights from analogue modeling using high resolution 3D digital image correlation

Edoseghe E. Osagiede[1,2,*], Matthias Rosenau[3], Atle Rotevatn[1], Rob Gawthorpe[1], Christopher A-L. Jackson[4], and Michael Rudolf[3]

[1]Geodynamics and Basin Studies Group, Department of Earth Science, University of Bergen, Allégaten 41, 5007, Bergen, Norway.

[2]Department of Geology, University of Benin, PMB 1154, Benin City, Nigeria.

[3]Lithosphere Dynamics, Helmholtz Centre Potsdam, German Research Centre for Geosciences (GFZ), Telegraphenberg, D-14473 Potsdam, Germany.

[4]Basins Group, Department of Earth and Environmental Sciences, The University of Manchester, Williamson Building, Oxford Road, Manchester, M13 9PL, United Kingdom.

Corresponding author: Edoseghe Edwin Osagiede (edoseghe.osagiede@uib.no; edoseghe.osagiede@uniben.edu)

Key Points:

- Inherited structural heterogeneities influence the pattern of strain localization and partitioning during rifting.
- Oblique normal- and strike- slip displacements are important strain accommodating mechanisms during oblique rifting.
- The interplay between the orientation, size, depth and geometry of inherited weak zone dictates their influence on rifting style.

Abstract

Pre-existing crustal structures have been shown to influence rifting, but the factors controlling their influence remain poorly understood. We present the results of surface strain analysis of a series of analogue rifting experiments designed to test the influence of the size, orientation, depth, and geometry of pre-existing crustal weak zones on strain localization and partitioning. We apply distributed basal extension to crustal-scale models which consist of a silicone weak zone embedded in a quartz sand layer. We vary the size and orientation (θ-angle) of the weak zone with respect to the extension direction, reduce the thickness of the sand layer to simulate a shallow weak zone, and vary the geometry of the weak zone. Our results show that at higher θ-angle ($\leq 60^{o}$) both small- and large-scale weak zones localize strain into graben-bounding (oblique-) normal faults. At lower θ-angle ($\leq 45^{o}$), small-scale weak zones do not localize strain effectively, unless they are shallow. In most models, we observe diffuse, second-order strike-slip internal graben structures, which are conjugate and antithetic under orthogonal and oblique extension, respectively. In general, the changing nature of the rift faults (from discrete fault planes to diffuse fault zones, from normal to oblique and strike-slip) highlights the sensitivity of rift architecture to the orientation, size, depth, and geometry of pre-existing weak zones. Our generic models are comparable to observations from many natural rift systems like the northern North Sea and East Africa, and thus have implications for understanding the role of structural inheritance in rift basins globally.

1 Introduction

Intra-continental rifting very commonly occurs along pre-existing crustal heterogeneities (e.g., McConnell, 1967; Dunbar & Sawyer, 1988; Daly et al., 1989; Versfelt & Rosendahl, 1989; Ring, 1994; Vauchez et al., 1998; Corti et al., 2003; Gibson et al., 2013; Brune et al., 2017). Such presumably weak heterogeneities include discrete faults (with limited width), diffuse shear zones (up to several 10s of km-wide) and mobile belts (up to 100s of km-wide), and orogenic structural templates, all of which create crustal-scale rheological and mechanical anisotropies (e.g., Daly et al., 1989; Ranalli & Yin, 1990). Numerous subsurface- and field-based studies suggest such pre-existing structures can influence the location, orientation, dimensions, segmentation, and interaction of subsequent rift-related structures (e.g., Daly et al., 1989; Bartholomew et al., 1993; Maurin & Guiraud, 1993; Maerten et al., 2002; Morley et al., 2004; Morley, 2010; Kirkpatrick et al., 2013; Fazlikhani & Back, 2015; Salomon et al., 2015; de Castro et al., 2016; Phillips et al., 2016; Fazlikhani et al., 2017; Dawson et al., 2018; Kolawole et al., 2018; Muirhead & Kattenhorn, 2018; Rotevatn et al., 2018; Collanega et al., 2019; Heilman et al., 2019; Osagiede et al., 2020a).

In many natural rifts like the northern North Sea Rift (e.g., Reeve et al., 2015; Phillips et al., 2016; Claringbould et al., 2017; Phillips et al., 2019; Osagiede et al., 2020a), East African Rift System (e.g., Daly et al., 1989; Morley, 1995; Heilman et al., 2019), Parnaíba Basin, Brazil (de Castro et al., 2016), Thailand rift basins (Morley et al., 2004), and East Greenland Rift System (e.g., Rotevatn et al., 2018), the influence of pre-existing crustal structures on strain localization during extension varies, (see Fig. 1). Whereas some pre-existing crustal structures clearly reactivate and control subsequent deformation, others seem to have limited or no influence. It is this variable effect of pre-existing structures on younger rift-related structures that we here refer to as *selective influence*. Although the influence of pre-existing crustal structures on strain localization in natural rifts is well recognized, the factors that control their observed selective influence remain poorly understood. Seismic reflection data suggest that the thickness and, to some extent, the depth of pre-existing crustal structures like shear zones seem to dictate their influence on the superposed rift structures (e.g., Reeve et al., 2013; Phillips et al., 2016; Osagiede et al., 2020a). Analogue and numerical simulations of rift processes provide valuable tools to validate such hypotheses.

Insert Figure 1

Scaled analogue or numerical models allow us to monitor the progressive crustal strain localization process and the development of rifts at high resolution in space and time. Over the past decades a growing number of analogue- (e.g., Withjack & Jamison, 1986; Allemand & Brun, 1991; Tron & Brun, 1991; Dauteuil & Brun, 1993; McClay & White, 1995; Bonini et al., 1997; Keep & McClay, 1997; Basile & Brun, 1999; Brun, 1999; Clifton et al., 2000; Michon & Merle, 2000; Corti et al., 2001; Chemenda et al., 2002; McClay et al., 2002; Bellahsen et al., 2003; Corti et al., 2003; Bellahsen & Daniel, 2005; Michon & Sokoutis, 2005; Sokoutis et al., 2007; Agostini et al., 2009; Autin et al., 2010; Henza et al., 2010; Aanyu & Koehn, 2011; Agostini et al., 2011; Autin et al., 2013; Chattopadhyay & Chakra, 2013; Tong et al., 2014; Bonini et al., 2015; Philippon et al., 2015; Zwaan et al., 2016; Zwaan & Schreurs, 2017; Molnar et al., 2019; Sani et al., 2019; Zwaan et al., 2019; Ghosh et al., 2020; Maestrelli et al., 2020; Molnar et al., 2020) and numerical- (e.g., Van Wijk, 2005; Dyksterhuis et al., 2007; Maniatis & Hampel, 2008; Allken et al., 2012; Brune et al., 2012; Brune & Autin, 2013; Brune, 2014; Brune et al., 2017; Deng et al., 2017; Duclaux et al., 2020) modeling studies have investigated the role of pre-existing structures on evolving rifts, addressing the role of orthogonal and oblique extension, and the effect of the orientation of pre-existing crustal and/or mantle weaknesses, the thickness of the brittle layer, brittle-ductile coupling, the presence or absence of weak lower crust, extension velocity, and multi-phase extension.

Most previous studies have focused on first-order attributes like the nature of pre-existing weak structures such as discrete (faults) versus distributed structures (e.g., Bellahsen & Daniel, 2005; Tong et al., 2014; Bonini et al., 2015; Deng et al., 2017), and the orientation (obliquity) of the inherited structure with regards to the extension direction (e.g., Withjack & Jamison, 1986; McClay & White, 1995; Michon & Sokoutis, 2005; Agostini et al., 2009; Autin et al., 2013; Molnar et al., 2019). With the progress made in seismic imaging of deeply buried structures located in crystalline basement, higher-order attributes such as the size, depth and shape of pre-existing structures are becoming evident (e.g., Phillips et al., 2016; Wrona et al., 2020; Osagiede et al., 2020a); such attributes have received little attention in modeling studies, thus little is known about how they influence the evolving rifts, especially in the context of pre-existing structures like crustal shear zones (here referred to as weak zones).

In this study, we investigate the controls that pre-existing crustal weak zones have on the strain localization process and development of rift-related structures during extension. We achieve this through a series of extensional analogue experiments that test how the (i) size, (ii) depth, and (iii) geometry of pre-existing crustal weak zones (specifically shear zones) affect their propensity to influence younger rift faults. We deploy state-of-the-art stereoscopic (3D) digital image correlation (DIC) technique that allows us to quantitatively assess the evolution of the model surface deformation and structural pattern at high resolution. Our results are of generic significance and have implications for understanding how pre-existing weak zones selectively influence younger rift faults in natural rift systems.

2 Experimental method and model design

2.1 Experimental setup

The experimental apparatus can be considered a pure shear extension experiment (Fig. 2). A basal neoprene foam block with dimensions of 50 x 50 x 12 cm is first compressed by 5 cm (i.e. down to an initial width of 45 cm) between a fixed and mobile wall, with open side walls, before placing the rock analogue materials on top of it. Subsequently, we start the model run by slowly moving the mobile wall at a constant rate of 0.005 mm/s, and releasing the compressed foam by a total of 5 cm, translating theoretically into c. 11% of extension during each model run. Due to some localization of extension at the model boundaries, the effective extension in the model domain is a bit less (c. 9 ± 1%) and distributed homogenously as verified by benchmarks (Appendix 1). The use of a basal foam in analogue model studies has the advantage of simulating distributed extension with a constant basal velocity gradient (Appendix 1), compared to the use of rigid base plates that typical serve to strongly localize basal extension (e.g., Schlagenhauf et al., 2008; Zwaan et al., 2019).

A side effect of using elastic materials to impose basal kinematic boundary conditions is the association of transverse contraction along with longitudinal extension. This “Poisson’s effect” may lead to a switch in simulated tectonic setting from crustal extension to strike-slip if the Poisson’s ratio is close to 50%, as often happens with a basal rubber sheet, for example (Bahroudi et al., 2003; Zwaan et al., 2019). However, in our model setup, lateral contraction of the basal foam block is c. 16% of its longitudinal extension (i.e., 0.8 cm contraction associated with 5 cm extension, Appendix 1) and therefore suitable for simulating crustal extension with only a minor contribution of transverse contraction.

In this study, our focus is on the surface deformation of the brittle crust; we do not explicitly model a ductile lower crust, which has been sufficiently addressed by previous analogue modeling studies (e.g., Allemand & Brun, 1991; Brun, 1999; Bellahsen et al., 2003; Zwaan et al., 2019). Our reference model setup therefore simulates an old and cold stable (e.g., Brun, 1999; Zwaan et al., 2019) or a highly coupled (e.g., Dyksterhuis et al., 2007) crustal/lithospheric setting. That is, our model setup does not capture the vertical rheological stratification that may characterize the crust, but rather focus on the lateral mechanical anisotropy induced by relatively local pre-existing weak zones like shear zones (e.g., Vauchez et al., 1998).

Insert Figure 2

2.2 Rock analogue materials

As a rock analogue material for the brittle upper crust, we used a mix of natural- and a few percent of black-colored, dry, quartz sand (type G12, Rosenau et al., 2018). This mixture provides an appropriate visual contrast that allows for the digital correlation of recorded images (e.g., White et al., 2001). The grain size is 100 – 400 µm, with an average of 240 µm. The bulk density of the sieved sand is about 1700 kg/m^3. The sand exhibits a frictional-Coulomb plastic behavior, with static and dynamic friction coefficients of 0.69 and 0.55, respectively, and a cohesion in the order of a few tens of Pascal (see Table 1) (Rosenau et al., 2018). Quartz sand like this has been widely used to represent brittle upper crustal rocks in numerous analogue models (Lohrmann et al., 2003; Adam et al., 2005; Panien et al., 2006; Schreurs et al., 2006, 2016; Klinkmüller et al., 2016; Ritter et al., 2016; Schellart & Strak, 2016; Del Ventisette et al., 2019).

We use viscoelastic objects made of Polydimethylsiloxane (PDMS) or silicone oil to represent pre-existing weak zones, simulating kilometer-scale shear zones within the brittle crust. While several methods permit simulation of weak zones into sand-based analogue models (e.g., Le Calvez & Vendeville, 2002; Zwaan et al., 2019), a major advantage of using silicone oil is that it can be easily moulded to produce a range of sizes and shapes that reflects a diverse range of natural weak zone geometries. The silicone oil has a density (ρ) of c. 960 kg/m^3, and a zero-shear viscosity (η) of c. 2.24 x 10^4 Pa s (Table 1) (Rudolf et al., 2016). As a Maxwell viscoelastic fluid, it has a linear viscous rheology (Newtonian) at relatively low strain rates as realized in our experiments, changing to a non-linear viscous rheology at much higher strain rates than achieved in this study (Rudolf et al., 2016). We choose this material for the weak zone because it can respond to the extension applied at the model base while maintaining its shape and height over the experimental time scale.

Table 1: Material properties

Brittle Layer (granular material)	**Quartz Sand 'G12'**
Grain size range (μm)[a]	100-400
Mean grain size (μm)[a]	240
Grain density (kg/m^3)[a]	2650
Sieved density (kg/m^3)[a]	1700
Coefficient[a]/Angle of internal peak friction	0.69/34.6°
Coefficient[a]/Angle of internal dynamic (sliding) friction	0.55/28.8°
Strain softening (%)	20
Cohesion (Pa)[a]	50 - 110
Weak zone (viscous material)	**Polydimethylsiloxane (PDMS) KORASILON G30M 'Silicone'**
Density ρ (kg/m^3)[b]	957.1
Viscosity η (Pa.s)[b]	2.24 x 10^4
Power-law stress exponent[b]	0.996 (quasi-Newtonian)

[a] Rosenau et al., 2018; [b] Rudolf et al., 2016

2.3 Scaling

To achieve analogue models that are applicable to nature, an adequate geometric (length), kinematic (time) and dynamic (stress) scaling between model and nature must be established (Hubbert, 1937; Ramberg, 1981; Mulugeta, 1988; see also review by Schellart & Strak, 2016). For proper dynamic scaling and similarity in the brittle regime, the following equation, relating material strength (here cohesion C) and gravitational stresses (or overburden pressure), should be satisfied:

$$C^* = \rho^* \times g^* \times l^* = \sigma^* \quad (1)$$

where C^*, ρ^*, g^*, l^*, and σ^* are the model vs. nature ratios (called 'scaling factors') for cohesion, density, gravity, length, and stress respectively. Since the experiment is carried out under normal gravitational field in the laboratory, g^* is 1, and Eq. (1) reduces to:

$$C^* = \rho^* \times l^* = \sigma^* \quad (2)$$

With setting up the model at laboratory scale we impose a geometric scaling factor (length ratio l^*) in the order of 10^{-5} to 10^{-6}, that is, 1 cm in the model represents c. 1 – 10 km in nature. The density ratio ρ^* is c. 0.7 (assuming an average density value to 2400 kg/m^3 for sedimentary and crystalline rocks in the upper crust). Therefore, dynamic similarity (from Eq. 2) is achieved with a material satisfying a cohesion ratio (C^*) that equals a stress ratio (σ^*) of 7 x $10^{-6 \text{ to } -7}$. Accordingly, our quartz sand with an average cohesion of a few tens of Pascal will be able to simulate brittle crustal rocks with cohesion in the range of approximately 10 – 100 MPa. This range is well within the range of cohesion values for brittle crustal rocks (e.g., Schellart, 2000; Klinkmüller et al., 2016; Schellart & Strak, 2016 and references therein).

Given that our model is dominated by brittle deformation whose behavior is therefore not time-dependent (as it would be for viscous models) we are free to choose a suitable time scale from dimensional consideration according to the equation:

$$T^* = \frac{l^*}{V^*} \quad (3)$$

where T^*, l^*, and V^* are the model vs. nature ratios of time, length, and velocity, respectively. We derive the scaling factor for time by solving eq. (3) for the following values: model "plate" velocity = 1.8 cm/hr, nature velocity = 3 mm/yr (e.g. average extension rate for the East African Rift; Saria et al., 2014), and length scale as above. Accordingly, we arrive at a time scaling such that 1 hr in our model scales up to ca. 2 – 20 Ma in nature.

We note that even if we consider that our models are brittle-dominated and display time-independent behaviour, the rheology of the weak zone material needs consideration in the context of its viscous behavior, as the expected strain rate defines how weak the crust is in the weak zone region compared to the normal crust. The viscous strength of any flowing material is the viscosity times the strain rate. For a strain rate of 10^{-5}/s as in our experiments (see appendix 2) it follows that the weak zone material strength is about 0.1 Pa, which is 100 to 10,000 times lower than the strength of the quartz sand layer that increases linearly with depth from cohesion values near the surface to about 700-800 Pa at the base of the 4 cm thick models. Therefore, we consider the contribution of the weak zone itself to the integrated strength of the model crust to be negligible. The integrated model crustal strength (i.e. the area beneath the strength profile) in the area underlain by the weak zone is proportional to the squared thickness of the layer above the weak zone (see Zwaan et al., 2020, for a geometric derivation of this scaling). Accordingly, for 1 cm- and 2 cm- thick weak zones in an overall 4 cm thick layer model crust, the integrated strength in the weak zone area is reduced to ca. 56% and 25% respectively, of the integrated strength of the normal (pristine or sand-only) model crust.

2.4 Model series design

We present a reference model (R), and ten main models grouped into five main series (A – E; Table 2). The reference model consists of a 4 cm-thick sand layer (without a pre-extension weak zone) directly coupled to the extending foam. Series A and B focused on testing the extent to which the size (small vs large, respectively) and the orientation of pre-existing weak zones control the pattern of strain localization and partitioning in the overlying cover. In Series C, we use the thickness of the overburden brittle-layer as a proxy to examine the influence of shallow vs. deep burial of pre-existing weak zones on the extent of strain localization in the overlying cover. Series D and E test the influence of the overall 3D geometry of pre-existing weak zones on deformation patterns during crustal extension. Details of the (i) orientation angle θ, of the weak zone with respect to the applied extension direction, measured clockwise (positive angle) or anti-clockwise (negative angle) (ii) dimension and geometry of the weak zone, and (iii) integrated strength in the area underlain by the weak zone, with respect to the normal model crust, for each model are provided in Table 2. In this paper, models where the weak zone is orthogonal to the extension direction (i.e., $\theta = 90^o$) are referred to as *orthogonal extension models*, whereas those with oblique weak zone vs. extension direction angles (i.e., $\theta = 60^o$ and 45^o) are referred to as *oblique extension models*. Note that in Series E model, the weak zone was curvilinear implying that about half of the weak zone is orthogonal to the extension direction ($\theta = 90^o$) and half is oblique to the extension direction ($\theta = 60^o$).

Table 2: Summary of experimental series

Experiment Series	**Model Run**	**Brittle Layer (G12 Sand) Thickness (cm)**	**Weak zone (silicone)**				**Strain Analysis (presented in this paper)**	
			Orientation, θ (w.r.t. extension direction)	**Dimension/Size** *Small = 30 x 1 x 1 cm* *Large = 30 x 2 x 2 cm*	**Weakness** (Integrated strength in weak zone area w.r.t. normal model crust)	**Geometry/Shape**	**Normal strain** E_n	**Shear strain** E_s
Reference	Model R	4	-	-	-	-	X	X
Series A	Model A1	4	90º	Small	56%	Cuboid	X	X
	Model A2	4	60º	Small	56%	Cuboid	X	X
	Model A3	4	45º	Small	56%	Cuboid	X	X
Series B	Model B1	4	90º	Large	25%	Cuboid	X	X
	Model B2	4	60º	Large	25%	Cuboid	X	X
	Model B3	4	45º	Large	25%	Cuboid	X	X
Series C	Model C	1.5	45º	Small	44%	Cuboid	X	
Series D	Model D1	4	- 60º	See Fig. 2f	≥ 56%	Triangular prism	X	
	Model D2	4	- 60º	See Fig. 2f	≥ 56%	Semi-cylindrical	X	
Series E	Model E	4	Curvilinear (see text)	See Fig. 2f	≥ 56%	Semi-cylindrical	X	

2.5 Surface deformation monitoring

We used a stereoscopic pair of two 12-bit, 29-megapixel monochrome CCD (charge-coupled device) cameras (LaVision Imager XLite 29M) mounted c. 1 m above the model surface with oblique viewing angles (Fig. 2d). Images were recorded at an image frequency of 0.05 Hz, corresponding to one image every 20 s, which, given the extension velocity (0.005 mm/s) of our models, represents one image per 0.1 mm of wall displacement.

To process the recorded images, we deployed a digital image correlation (DIC) technique, also known as particle imaging velocimetry (PIV), that allows us to monitor the surface deformation at high spatial and temporal resolution (e.g., White et al., 2001; Adam et al., 2005; Dautriat et al., 2011; Ge et al., 2019). We used commercial LaVision Davis 10 software employing a least-squares-method (LSM) to calculate the three-component deformation field between successive images. DIC processing was done at increments comparing every 10th image, representing 1 mm of sidewall displacement. We find that this interval is not only computationally convenient, but also provides adequate information on the evolution of strain within our models at a high spatial and sufficient temporal resolution. To avoid the boundary effects, and further optimize computation time, DIC processing on the raw images was restricted to the central part of the model ('area of interest') by means of a rectangular mask (see Figs. 2b and 3).

The DIC results we present in this study are based on time-series of the 3D cumulative surface displacement field, where incremental displacements are summed up in a Lagrangian reference frame. From the 3D surface displacement field, the in-plane (2D horizontal) cumulative normal- (ε_n) and shear- (ε_s) strains were derived. The ability to decompose strain into normal and shear components highlight the key strength of the DIC analysis deployed in this study, in comparison to the numerous previous analogue models where deformation analysis has been mostly based on qualitative (rather than quantitative) visual inspection of model surface deformation at a much lower spatial and temporal resolution. The computed strain distribution allows us to quantitatively assess the geometry and pattern of strain distribution of extension-related structures in our models at unprecedented resolution.

3 Model Results

The results are presented first in sections 3.1 – 3.4 based on the different experimental series. Within each section, we first present the final stage (c. 11% extension) of the model evolution by means of the surface fault pattern and the DIC-derived surface normal strain (ε_n). We also present the DIC-derived surface shear strain (ε_s) of the reference model, and Series A and B models, highlighting the oblique nature of first-order and secondary strike-slip structures. We finally provide cumulative model surface subsidence profiles illustrating the temporal evolution of topography. In section 3.5 we briefly highlight temporal aspects of structural evolution and in section 3.6 we quantify the obliquity of normal faulting in selected models. All data underlying this study and additional results of the DIC processing (not discussed here) are provided open access in Osagiede et al. (2020b).

3.1 Reference model R: Brittle-only (homogenous layer, no weak zone)

The final stage (c. 11% extension) of the reference model surface is characterized by the occurrence of faults only along the boundaries of the model due to boundary effect resulting from the discontinuity between the sand layer and the model sidewalls (Fig. 3a). There is no localization of deformation in the central portion of the model. Instead, distributed, diffuse normal strain bands (c. 10% strain), orthogonal to the extension direction develop (Fig. 3b) with no associated shear strain (Fig. 3c). We interpret these diffuse strain bands as the equivalent of the distributed faulting reported in previous analogue models by both Schlagenhauf et al. (2008) and Zwaan et al. (2019). Diffuse strain plausibly a consequence of the larger grain size of the sand used in our setup (our mean grain size of 240 µm vs. their c. 120 µm) and the higher amount of extension applied in their models (our c. 11% vs. their ≥ 13%). Apart from the diffuse strain bands, there is no significant shear strain localization in the model (Fig. 3c). The result of the reference model is important in this study because it allows us to differentiate the inherent model observations that are due to (i) the absence of a pre-existing weak zone and (ii) edge and/or basal boundary conditions associated with the overall model setup. The diffuse strain bands are interpreted to result from the distributed basal extension boundary condition (i.e. brittle layer directly on basal foam) in our model setup, and are not considered or interpreted further in this paper.

Insert Figure 3

3.2 Experimental Series A and B: small- vs. large- sized weak zones with variable orientation

The model surface deformation after the final stage (c. 11%) extension of Models A1 (small weak zone, $\theta = 90^o$), A2 (small weak zone, $\theta = 60^o$), B1 (large weak zone, $\theta = 90^o$), B2 (large weak zone, $\theta = 60^o$) and B3 (large weak zone, $\theta = 45^o$) are characterized by surface displacement along normal faults that bound model rift-related graben (herein referred to as graben-bounding faults) and which form directly above and parallel to the underlying weak zone (Figs. 4a, 4f, 5a, 5f, and 5k). The graben-bounding faults are well constrained as localized, high normal strain zones (≥ 20%, Figs. 4b, 4g, 5b, 5g, and 5l). The final stage of Model A3 (small weak zone, $\theta = 45^o$) differed to other models in that a rift-related graben structure did not develop (Fig. 4k and 4l). This suggests that the weak zone in this model does not weaken the brittle layer sufficiently to allow for strain localization and surface displacement on graben-bounding faults under moderate obliquity.

In the orthogonal extension models (A1 and B1), the graben-bounding faults are through-going with an overall orientation that is perpendicular to the extension direction, except around the fault tips where the fault geometry slightly deflects outward (Figs. 4a, 4b, 4d, 5a, 5b and 5d). The fault tip deflection is most likely a boundary effect that is due to both the transverse contraction (Poisson's effect) imposed by the basal foam, and the slope of the sand layer on the unconfined sides of the model-setup (Fig. 2a and 3). In Model B1, intra-graben faults that are parallel but antithetic to the main graben-bounding faults also develop, resulting in the formation of a central horst separating double marginal grabens (Figs. 5a, 5b and 5d). Similar deformation pattern where double marginal grabens develop have been previously described in numerous analogue studies (e.g., Allemand & Brun, 1991; Keep & McClay, 1997; Corti, 2004; Schreurs et al., 2006; Corti, 2012; Zwaan et al., 2019). In the oblique extension models (A2, B2, and B3), the resulting graben-bounding faults are generally oblique to the extension direction, except at the lateral tips of the faults where their geometry deflects, becoming near-orthogonal to the extension direction (Figs. 4f, 4g, 4i, 5f, 5g, 5i, 5k, 5l and 5n). The normal strain component shows that in some of the models, specifically Models B1 and B2, there are ellipsoidal-shaped zones of approximately zero-strain (little or no deformation) in the immediate footwall and/or hangingwall of the graben-bounding faults (blue zones in Figs. 5b and 5g). These zones are here referred to as strain shadows (Figs. 5d and 5i) (e.g., Ackermann & Schlische, 1997; Cowie, 1998; Gupta & Scholz, 2000; Soliva et al., 2006; Deng et al., 2017).

Insert Figure 4

Insert Figure 5

The shear strain component of the deformation provides insight into the role of oblique slip and strike-slip during rift evolution, particularly under oblique extension (Withjack & Jamison, 1986). In the orthogonal extension models (Models A1 and B1), the pattern of the shear strain distribution along the graben-bounding faults is largely chaotic in the central part of the faults, and more systematic only at the fault tips (Figs. 4c and 5c). The chaotic shear strain pattern reflects pure-dip slip in the central part of the graben-bounding faults. Some systematic oblique slip is indicated at the fault tips which is consistent with lateral contraction imposed on the model by the basal foam. Within the graben (especially Model A1), there are poorly developed, diffuse shear strain zones (c. ± 0.3%). These were not obvious in the normal strain pattern indicating their pure strike-slip nature. We interpret these as sets of conjugate strike-slip faults formed in response to the small lateral contraction imposed by the basal foam in an overall pure shear regime (see Appendix 3). These poorly developed conjugate shears within the graben are typically not observed in natural rifts, and thus are considered here as basal boundary effects, and are not considered further in this paper.

In oblique extension models A2, B2 and B3, the overall shear strain distribution is generally similar and consistent with strain partitioning in transtensional kinematics (see Appendix 3). The graben-bounding faults are consequently characterized by a minor component of dextral shear motion (Figs. 4h, 5h and 5m). Within the graben, en échelon, sigmoidal zones of sinistral (i.e. antithetic) shear developed (especially in Models A2 and B3). These intra-graben structures did not accommodate vertical surface displacement as they are not apparent in the normal strain component of the model deformation, indicating that they are purely strike-slip structures. We interpret them as antithetic Riedel (R') shears related to the simple shear component of transtension. These R' shears are even seen in Model A3 (Fig. 4m), although no main graben developed as observed from the model surface and normal strain analysis (see Figs. 4k and 4l). The overall en échelon arrangement of the R' shears is parallel to the underlying weak zone, whereas the individual R' shears are near-orthogonal to the extension direction.

The width of the rift-graben is approximately the same (c. 4cm) for Models A1 and B1, irrespective of the size of the underlying weak zone (compare Figs. 4a and 5a), whereas it is slightly narrower with decreasing θ-angle (compare Figs. 5a, 5f and 5k). The width of the rift-graben is unaffected by the size of the weak zone because the graben width is not only dependent on the thickness of the brittle layer above the weak zone and the dip of the graben-bounding faults, but also on the width of the weak zone (Corti, 2004) (see Appendix 4). Time-series cross-sectional profiles of the models show that the subsidence is symmetric within the rift-graben (Figs. 4e, 4j, 5e, 5j and 5o), except for Model A3 where the profiles are flat because no graben developed in the model (Fig. 4o). Whereas the model surface outside the model rift-graben generally subsides at rather constant rates (equidistant horizontal profile segments) consistent with distributed thinning, the rift-graben floors show indications of variable subsidence rates over the model run. The absolute degree of subsidence varies between models, generally increasing with increasing size of the underlying weak zone (compare Figs. 4e and 5e) and decreasing with decreasing θ-angle (compare Figs. 5e, 5j and 5o). The subsidence rate is positively correlated to the amount of vertical displacement accommodated by the graben-bounding faults. Interestingly, the subsidence profile also show zones of relative footwall uplift with magnitudes that positively correlate with amount of vertical displacement of the associated graben-bounding faults (Figs. 4e, 5e, 5j).

3.3 Experimental Series C: thin brittle layer

We here compare an additional model (Model C) where the thickness of the brittle layer was reduced to 1.5 cm with Series A models that had 4 cm-thick brittle layers. Model C has a small (1 cm-thick) weak zone that is oriented $\theta = 45^{o}$. The only difference between the setup of Model C and A3 is the thickness of the brittle layer. Thus, the brittle layer thickness above the weak zone is 0.5 cm and 3 cm for Model C and A3, respectively. In the final stage of extension, Model C is characterized by surface displacement and strain localization along graben-bounding faults that form directly above and parallel to the underlying weak zone (Figs. 6a–c). This observation provides insight on the effect of the depth of the weak zone, since Model A3 with a thicker overburden brittle layer did not localize deformation (compare Figs. 6a and 4k). The graben structure in Model C is c. 1 cm and narrower than those formed in Series A. Furthermore, the normal strain distribution along the graben-bounding faults is characterized by several local maxima (Figs. 6b–c). The location of these strain maxima coincides with the termination zone of the diffuse strain bands on the obliquely oriented graben-bounding faults, and thus could be considered a boundary effect. Time-series cross-sectional profiles of the model show that the subsidence is symmetric within the rift-graben (Fig. 6d).

Insert Figure 6

3.4 Experimental Series D and E: variable weak zone geometry

Figure 8 shows the results of the final stage (c. 11%) extension of three models (Models D1, D2, and E) with different weak zone geometries, simulating a range of cross-sectional and plan-view geometries that pre-existing weak zones may exhibit in nature. Overall, the deformation patterns of these models are more complex compared to the models in Series A – C, in which we used geometrically simple, cuboid-shaped weak zones.

In Model D1 with an upward pointing triangular prism-shaped weak zone, the normal strain distribution across the graben structure is quite asymmetrical (Figs. 7a–b). The ‘southern’ boundary of the graben is characterized by a through-going border fault, with a zig-zag geometry consisting of relatively longer segments that are parallel to the underlying weak zone, and shorter jogs that are subparallel to the extension direction (Fig. 7c). The zig-zag geometry reflects growth by the (at-surface) linkage of initially isolated weak zone-parallel fault segments. However, the strain distribution pattern along the ‘northern’ boundary of the graben is more complex. Unlike the southern boundary, the northern boundary is characterized by a wider zone of faulting, with a dominant right-stepping en échelonéchelon faulting style (Figs. 7a–c). The en echelon fault set consists of individual fault segments which are oriented sub-perpendicular to the extension direction but is overall aligned parallel to the underlying weak zone. Time-series cross-sectional profiles show asymmetric subsidence within the rift-graben, broadly reflecting a half-graben structure (Fig. 7d).

Insert Figure 7

In Model D2 with a broader, deformed semi-cylindrical-shaped weak zone, normal strain distribution on the borders of the graben structure is near-symmetrical (Figs. 7e–f). This differs from the asymmetric strain distribution observed in Model D1. In contrast to the discrete graben-bounding faults observed in Series A – C models, the graben in Model D2 is bounded relatively wide (c. 2.5 cm) deformation (fault) zones on both margins (Figs. 7e–f). The wide fault zones are characterized by variable fault styles, including; subparallel fault sets, anastomosing faults (*sensu* Peacock et al., 2016), and right-stepping en échelon faults (within the ‘northern’ border fault zone, similar to Model C8) (Fig. 7g). Within the graben, discrete intra-graben fault develops parallel to the underlying weak zone. The intra-graben fault accumulates higher amount of deformation (c. ≥ 20% strain) compared to the border fault zone

(Fig. 7f). The time-series cross-sectional profiles of the graben subsidence is symmetrical, unlike that of Model D1 (Fig. 7h). Also, the symmetry of the subsidence profile is characterized by a 'dual slope' and differs from the 'single slope' symmetry of Series A – C models (compare Fig. 7h with profiles in Figs. 4, 5, and 6).

Model E contains a weak zone that has a deformed semi-circular cross section, but curvilinear planform geometry. The normal strain distribution is similar to Model D2, with wide (c. 2.5 cm) fault zones bounding the rift-graben structure (Figs. 7i–j). The wide fault zones also exhibit variable fault styles (Fig. 7k). Like Model D2, the intra-graben fault is parallel to the underlying weak zone, and accumulates higher amount of deformation compared to the border fault zone (Fig. 7j). However, the development of the intra-graben fault is only limited to the eastern portion of the graben structure that is oblique to the extension direction, and do not extend to, or develop in, the western portion that is perpendicular to the extension direction. The time-series cross-sectional profiles of the graben subsidence is symmetrical, and identical to that of Model D2 (Fig. 7l).

3.5 Temporal evolution of model structures

To illustrate the temporal evolution of the model structures, we briefly present the early (extension = 2.2%), intermediate (extension = 6.7%), and final (extension = 11.1%) stages of normal strain evolution of some Series A and B models (Fig. 8). The timing of faulting and amount of strain accommodated by the faults varies in these models. For example, whereas the graben-bounding faults in Model A1 (small weak zone, $\theta = 90^o$) accommodated only c. 5% strain at the early stage of extension, its equivalent in Model B1 (large weak zone, $\theta = 90^o$) already accommodated up to 15% strain by the same stage (compare Figs. 8a and c). Similarly, the graben-bounding faults in Model B2 (large weak zone, $\theta = 60^o$) accommodated more strain than in Model A2 (small weak zone, $\theta = 60^o$) at the same stages (compare Figs. 8b and d).

Furthermore, Comparing Models A1 and A2 show that whereas graben-bounding faults initiated early (during the early stage) as through-going faults in Model A1, they initiated later as mostly isolated, en échelon faults in Model A2 (compare Figs. 8a and b). The en échelon faults are left-stepping and aligned parallel to the underlying pre-existing weak zone (Fig. 8b).

There is a two-phase sequential evolution of the rift-related faults in Model B1. The first phase is characterized by the initiation and accumulation of normal strain (vertical displacement) on the graben-bounding faults during the early stage of the model deformation, and the second phase is characterized by the initiation and accumulation of normal strain on antithetic intra-graben faults during the intermediate – late stage (Fig. 8c). A similar, but less-well developed two-phase development of the faults is also observed in Model B2 (Fig. 8d).

Insert Figure 8

3.6 Quantifying the normal vs. shear strain on model structures

To quantify the obliqueness of normal faults we analyse the relative amount of normal vs shear components of strain accommodated by the graben-bounding faults and discrete intra-graben faults (when formed). The finite normal and shear strain are plotted along profiles that are parallel to the model extension direction (Fig. 9). The plots highlight the overall style of the graben-bounding faults, consisting mainly of either narrow (single) border faults (Models A1, A2, B1, B2, B3, and C), wide border fault zones (Models D2 and E), or both (Model D1) (Fig. 9). In Model A3, both the normal and shear strain lines are flat because strain did not localize in the model domain (Fig. 9i). These styles are consistent with the observations from the model surface and strain maps of the respective models (Figs. 4, 5, 6, and 7).

In the orthogonal extension models (Models A1, B1, and the orthogonal half of Model E), the strain accommodated by the graben-bounding and intra-graben faults is 100% normal strain and zero shear strain consistent with pure normal faulting (Figs. 9a–c). In the oblique extension models (Models A2, B2, B3, C, D1, D2, and the oblique half of Model E), the strain accommodated by the graben-bounding and intra-graben faults compose of both normal and shear components with a variable relative ratio between the models (Figs. 9d–h, j–k). In Model A2, the finite normal strain on the graben-bounding fault is c. 0.11, whereas the shear strain is c. 0.01, implying that the shear strain is approximately one-tenth of the total strain on the fault (Fig. 9e). For Model B2, normal strain is c. 0.4, and shear strain is c. 0.1, implying that the shear strain is approximately one-fifth of the total strain on the fault (Fig. 9f). For Model B3, normal strain is c. 0.19, and shear strain is c. 0.06, implying that the shear strain is approximately one-fourth of the total strain on the fault (Fig. 9j). For Model C, the values of normal and shear strain are approximately the same as in Model B3, and shear strain is about one-fourth of the total strain on the fault (Fig. 9k). For Model D1, normal strain on the narrow border fault is c. 0.26, and shear strain is c. 0.06, implying that the shear strain is approximately one-fifth of the total strain on the fault (Fig. 9g). For Model D2, average normal strain on the wide border fault zone is c. 0.15, and average shear strain is c. 0.04, implying that the shear strain is approximately one-fifth of the total strain on the fault (Fig. 9h). Normal strain on the intra-graben fault is c. 0.27, and shear strain is c. 0.18, implying that the shear strain is approximately two-fifth of the total strain on the fault (Fig. 9h). For the oblique ($\theta = -60^{o}$) half of Model E, the normal and shear strain patterns are identical to Model D2, underpinning the reproducibility of the models (compare Figs. 9d and h). Consequently, the normal and shear strain on the wide border fault zone and intra-graben fault in Model E and D2 are similar.

Insert Figure 9

In summary, in the orthogonal extension models, shear strain does not contribute to the total strain accommodated by the graben-bounding and intra-graben faults, except at the fault tips as observed in the strain maps described earlier (see Figs. 4c and 5c). These faults are orthogonal to the extension direction. In the oblique extension models, when $\theta = \pm 60^{o}$ (low obliquity), shear strain account for only c. 20% (one-fifth) of the total strain accommodated by the graben-bounding faults and 40% (two-fifth) of the total strain accommodated by the intra-graben fault. When $\theta = 45^{o}$ (moderate obliquity), the amount of shear strain on the graben-bounding faults increases to c. 25% (one-fourth) of the total strain.

4 Discussion

4.1 Comparison with previous analogue and numerical modeling studies

Observations from our models are broadly consistent with previous studies. Here, we briefly compare our key observations with observations from previous modeling studies and highlight the similarities and differences, where applicable.

First, the varying influence of a pre-existing crustal weak zone because of its orientation or depth compares well with previous models. For example, the ability of a weak zone to localize deformation is strongly influenced by the orientation of the crustal weak zone with respect to the model-extension direction, i.e., it localizes more when it is orthogonal (i.e., optimally oriented) and less with increasing obliquity (e.g., analytical solution by Ranalli & Yin, 1990; and analogue models by Zwaan & Schreurs, 2017; Molnar et al., 2019; Zwaan et al., in review). Also, our observation that a shallow weak zone (thin crustal cover) localizes more strain than a deeper weak zone agrees with previous analogue model results by Sokoutis et al. (2007). The observation from our model on the effect of the depth of the weak zone on the width of the rift-graben is comparable to that of Dyksterhuis et al. (2007). That is, a shallower weak zone results in a narrower graben width. This is because a shallow weak zone reduces the effective thickness of the brittle layer above the weak zone (e.g., Allemand & Brun, 1991; Brun, 1999; Dyksterhuis et al., 2007). This is in line with predictions from mechanical models which suggest that the width of a rift graben decreases with decreasing effective elastic thickness of the crust (Scholz & Contreras, 1998). The observation that the graben width narrows due to decreasing θ-angle (increasing obliquity) of the weak zone agrees with previous analogue modeling studies (e.g., Tron & Brun, 1991; Clifton et al., 2000; Zwaan et al., 2016). This is plausibly due to the increasing steepness/dip of the graben-border faults as they accommodate oblique-slip (e.g., Tron & Brun, 1991; Zwaan et al., 2016).

Second, the two-phase temporal evolution of rift-related faults (early graben-bounding faults vs. late intra-graben structures) in our models compares well with the early boundary faults and later internal faults observed in the orthogonal and low to moderate oblique rift analogue models of Agostini et al. (2009). This reflects the progressive migration of strain from the borders of the rift-graben towards the center of the graben (Agostini et al., 2009). However, in our models, the intra-graben (internal) faults are less-well developed and thus generally poorly expressed in the model surface (e.g., Figs. 5a and f) compared to those generated by Agostini et al. (2009) and Philippon et al. (2015). This difference is likely due to a combination of factors including, (i) the difference in the model setup and boundary conditions (e.g., brittle-ductile in their models vs. brittle-only in our model), (ii) the intrinsic strain-localization properties of the brittle material (coarse quartz sand in our model vs. fine-grained K-feldspar powder in their models), and (iii) the amount of applied extension (c. 11% in our model vs. approximately double in their models).

Third, the partitioning of deformation (in terms of both fault orientation and sense of fault slip) between the border faults and intra-graben structures under our low ($\theta = 60^{o}$) and moderately ($\theta = 45^{o}$) oblique extension is consistent with several previous models. In terms of fault orientation, the graben-bounding faults are oriented obliquely to the extension direction, whereas the intra-graben structures (consisting of en échelon R' shears) are approximately orthogonal to the extension direction. Such variability in the orientation of the border- vs. internal- structures have been observed in many previous low to moderate oblique-rifts analogue models (e.g., Withjack & Jamison, 1986; Tron & Brun, 1991; McClay & White, 1995; Bonini et al., 1997; Corti, 2008; Agostini et al., 2009; Autin et al., 2010; Philippon et al., 2015; Zwaan et al., 2016; Sani et al., 2019).

In terms of the sense of slip, an advantage of the high resolution DIC technique we deploy is that it allows even low strains (not captured by visual inspection) to be quantitatively decomposed into the normal- and shear- components based on the 3D displacement field. Thus, both the normal and shear sense of slip on the border- and internal- structures are constrained in our oblique extension models (Figs. 4, 5, and 9). Our data show that the border faults are oblique to the extension direction, and accommodate a major (80 – 75%) normal- and minor (20 – 25%) shear- components of strain, indicating they are oblique-slip faults, rather than pure dip-slip. Similar oblique-slip sense on faults striking oblique to the extension direction has been interpreted qualitatively in previous analogue models (e.g., Withjack & Jamison, 1986; Tron & Brun, 1991; Corti et al., 2007; Agostini et al., 2009; Corti, 2012; Molnar et al., 2019; Ghosh et al., 2020). Surprisingly, the extension-orthogonal, en échelon internal structures in our oblique extension models are pure strike-slip, differing from the dip-slip (vertical displacement) interpreted in earlier analogue (e.g., Corti, 2008; Agostini et al., 2009; Philippon et al., 2015) and numerical models (e.g., Brune, 2014; Duclaux et al., 2020). This difference can again possibly be explained by the difference in the amount of applied extension, which is comparably small (about half) in our study. For example, Agostini et al. (2009) showed that at low to moderate obliquity, the internal-rift faults only started accommodating vertical displacement and thus detectable surface expression after c. 12.5% of extension, which is higher than the total extension in our models. Similar oriented en-échelon internal structures but interpreted as normal faults are detected in numerical simulations at about 4% (Duclaux et al., 2020) to 20%

(Brune, 2014) extension. Duclaux et al. (2020) describe rotation of these structures in a synthetic sense with respect to the overall transtensional shear sense which would imply these normal faults have an antithetic strike-slip component as seen in our analogue models. The simulations of Brune (2014) suggest a set of strike-slip faults, where one is sub-parallel to the normal faults and one more oblique. We here infer that the internal structures possibly initiate as pure strike-slip (R' shear) structures (largely invisible to traditional monitoring techniques), which will later rotate and evolve to mainly dip-slip faults as extension increases (c. >10% extension) and strain migrates to the center of the rift-graben. It is however noteworthy that material properties controlling strain localization (i.e. strain weakening parameters) may significantly differ between nature, analog and numerical models and thus the evolution may only qualitatively follow the here suggested path. In any case, the application of the DIC technique in our analogue models thus provides new insights into the early-stage development of these internal rift structures that are not resolvable in previous analogue modeling studies using traditional visual inspection (e.g., Agostini et al., 2009; Philippon et al., 2015).

Lastly, the along-strike slip variation that characterizes the extension-orthogonal graben-bounding faults in our orthogonal extension models, i.e., pure dip-slip at the center of the faults and opposing sense of oblique-slip at the fault tips resemble observations from previous analogue- (Corti et al., 2013; Philippon et al., 2015) and numerical- (Maniatis & Hampel, 2008) models. However, in the previous models the opposing sense of oblique-slip kinematics at the fault tips converges towards the center of the individual faults (see Philippon et al., 2015), whereas in our model, it diverges away from the fault center (Figs. 4d and 5d). While convergent slip along single faults can be understood in terms of stretching with volume conservation (i.e. Poisson effect), divergent slip as observed in our models is interpreted as a boundary effect. More specifically, this likely relates to the inward drag of the deforming footwall block because of its direct frictional coupling to the laterally shortening basal foam while the hangingwall block, underlain by silicone, is decoupled from the foam and behaves like a more rigid block, resisting lateral shortening.

4.2 Controls on strain localization above pre-existing weak zones in natural rift systems

Our models provide insights into the way in which pre-existing weak zones may influence the structural style and drive strain localization during extension. During extension, the presence of an underlying pre-existing weak zone results in the development and localization of strain on graben-bounding faults and fault zones that form in the brittle cover, in all but one of the simulated scenarios (Model A3) (Figs. 4, 5, 6, and 7).

In experimental Series A and B, in which the size and orientation of the weak zone were varied, we observe that strain preferentially localized on graben-bounding faults in the brittle cover when the weak zone is oriented at $\geq 60^{o}$ to the extension direction, irrespective of the size of the weak zone (Figs. 4a–j and 5a–j). When the weak zone is oriented 45^{o} to the extension direction, the presence of the large weak zone (Model B3) resulted in strain localization along graben-bounding faults, whereas the small weak zone (Model A3) did not (Figs. 4k and 5k). This suggests that the control exerted by the size of pre-existing weak zones becomes increasingly more important with increasing obliquity of the weak zone with respect to the regional maximum extension direction. As the angle between the orientations of pre-existing weak zone and the extension direction reduces ($\theta \leq 45^{o}$), smaller-scale weak zones are less likely to locally perturb the regional stress field and localize strain, whereas, larger-scale weak zones may still localize strain at a much lower angle of orientation with respect to the extension direction. Ranalli and Yin (1990) presented detailed analytical solutions that demonstrates that the critical differential stress ($\sigma_1 - \sigma_3$) required for strain localization and eventual faulting on a plane parallel to a pre-existing strength anisotropy (i.e. weak zone) is dependent on: (1) the material parameters and layering, which controls the yield stress curve/strength profile, and the integrated strength in the vicinity of the anisotropy, compared to that of the homogenous, pristine column of the simulated crust (as quantified in Table 2, see also Fig. 2e), and (2) the orientation of the strength anisotropy, that is, there is a maximum orientation with respect to the principal extension direction (as a function of the integrated strength), beyond which strain localization is no longer possible along the anisotropy.

Comparing the results of Model A3 and Model C provides insight on the possible role of the depth of pre-existing weak zones on normal fault evolution, since the size (small) and orientation ($\theta = 45^{o}$) of the weak zone are the same, but Model C has a thinner brittle layer. In contrast to the lack of graben-bounding faults in the model with the thicker brittle layer (Model A3; Figs. 4k–o), strain localization on graben-bounding faults occurs above the weak zone in the thinner brittle layer (Model C; Figs. 6a–d). This suggests that a shallow pre-existing weak zone is more likely to localize strain in the brittle cover compared to a deep weak zone. Again, this is in strong agreement with Ranalli and Yin (1990), where they showed that critical differential stress increases with depth, implying that a lesser critical differential stress is required for strain to localize in the vicinity of shallow weak zones compared to deeper weak zones.

Our model observations correlate well with observations in many natural rifts such as the northern North Sea Rift (e.g., Phillips et al., 2016; Phillips et al., 2019; Osagiede et al., 2020a), Taranaki Basin, New Zealand (Collanega et al., 2019), and East African Rift (e.g., Daly et al., 1989; Morley, 1995), where some underlying pre-existing shear zones influenced the location, segmentation, and geometry of subsequent rift-related structures, whereas others had limited or no influence. For example, to the south of the western branch of the East African Rift System, the Rukwa-Malawi Rift segments preferentially developed along the large-scale NW-SE-trending inter-cratonic Ubendian mobile belt consisting of amalgamated Precambrian shear zones, whereas the N-S-trending Kenya Rift cross-cut the similar, but smaller-scale NW-SE-trending Aswa Shear Zone (see Fig. 1d) (e.g., Daly et al., 1989; Morley, 1995; Theunissen et al., 1996). More specifically, our work suggests that this selective influence of pre-existing weak zones on strain localization during extension is controlled by a complex interplay between the orientation, size, and depth of occurrence of the weak zones (Fig. 10). This conclusion supports previous suggestion by Phillips et al. (2016) where only 1-2 km thick (and not thin c. 100 m) Devonian shear zones preferentially reactivated and influenced younger rift faults in the northern North Sea. Similarly, Osagiede et al. (2020a) report that the Utsira Shear Zone (with a thickness > 3 km) locally perturbed the regional stress field during the Middle Jurassic – Early Cretaceous rift phase in the northern North Sea, thus influencing the geometry and growth of the cover rift faults, whereas the Heimdal Shear Zone (< 1 km-thick) had no influence on cover faults (see Fig. 1b).

Insert Figure 10

4.3. Influence of pre-existing weak zones on overall rift architecture

4.3.1 Influence on the development and timing of rift structures

In the models in which the underlying weak zone induces strain localization, the resulting graben is broadly parallel to the weak zone. However, the graben-bounding faults exhibits a range of styles from discrete through-going border faults that mimic the orientation of the weak zone (especially in orthogonal extension models), to individual en échelon fault segments that may be oblique to the weak zone (in some oblique extension models) (compare Figs. 8a and b). En échelon faults are characteristic of oblique extension and are observed in several oblique rift modeling studies (Withjack & Jamison, 1986; Tron & Brun, 1991; McClay & White, 1995; Clifton et al., 2000; Van Wijk, 2005; Agostini et al., 2009; Zwaan et al., in review). Overall, the correlation between the location, segmentation and orientation of the graben-bounding faults and the underlying weak zone indicates that the growth and geometry of the rift normal faults was strongly influenced by the weak zone (e.g., Collanega et al., 2019; Osagiede et al., 2020a).

Our quantitative model results provide new insights into how pre-existing weak zones control the timing of fault development in rifts. We find differences in the timing of faulting and the amount of strain accommodated by graben-bounding faults, as a function of either the orientation, size, or the depth of the weak zone. Graben-bounding faults nucleate earlier and accommodate more normal strain in orthogonal extension models compared to oblique extension models, where a complementary part of the strain is accommodated by oblique slip and intra-graben strike-slip (cf. Model A1 and A2; Figs. 8, 9). For models with the same weak zone orientation, the graben-bounding faults nucleate earlier for the thicker and/or shallower weak zone and accumulate more strain causing more pronounced strain shadows (cf. Model A2 and B2; Figs. 8b and d, 5g).

4.3.2 Influence on the style of bounding fault system

We observe that the 3D geometry of the underlying weak zone dictates whether strain localizes on either (i) narrow, discrete faults, or (ii) wide, diffuse fault zones, which ultimately bound rift-related graben. In many natural rift systems, for example the North Sea, pre-existing weak zones (e.g. ductile shear zones) exhibit a range of map-view geometries, from largely linear (e.g., Hardangerfjord Shear Zone) to curvilinear (e.g., Utsira Shear Zone) (Fig. 1a). In this study, we did not attempt to directly simulate any specific natural 3D weak zone geometry due to the complexity of these geometries in nature. However, we used four simplified, generic weak zone geometries in our models (see Table 2 and Fig. 2f). All models in Experimental Series A, B and C, where rift graben developed, were characterized by near-symmetrical strain localization on very narrow zones at the margins of the graben, resulting in a single or segmented border faults (Fig. 4, 5, 6, and 9). In all these models, the same weak zone geometry that simulates a block-like weak zone was used, and thus provides evidence of a striking relationship between the geometry of the weak zone and the distribution of strain.

Conversely, in Experimental Series D and E where we used weak zone geometries that simulated anticlinal weak zones, strain at the graben margins was more diffuse, resulting in a more structurally complex rift architecture characterized by the development of fault zones (and not a single-fault) on both margins (Fig. 7 and 9). These fault zones are characterized by a range of fault styles, including, near-parallel-, en échelon-, and anastomosing fault sets. Furthermore, the observed differences in the strain distribution in experimental Series D and E appears to also be related to whether the anticlinal geometry is ‘tight’ (Model D1), or ‘gentle’ (Models D2 and E) (Fig. 7). These results suggest that rift architecture is at least partly controlled by the 3D geometry of the pre-existing weakness.

4.3.3 Influence on strain partitioning under oblique extension

We have also observed significant strain partitioning in the oblique extension models, suggesting that oblique-slip and strike-slip are important mechanisms in the development of oblique rifts (e.g., Figs. 4h and 5m). A well-documented example is the NW-SE-trending Gulf of California, Mexico. Withjack and Jamison (1986) compared the pattern of faulting and strain partitioning in their analogue and analytical models to observations of a second rifting episode characterized by both normal to oblique-slip, and strike-slip faulting in the Gulf of California. Based on this comparison, they inferred that the pattern of faulting and strain partitioning observed in the Gulf of California best fits with an oblique rift system where the rift trend is c. 30^{o} to the relative displacement direction. The Gulf of California is therefore a highly oblique rift system where fault slip data show that E-W extension is accommodated by both oblique-slip (majorly dip-slip with minor dextral component) dominating the rift margin faults, and strike-slip dominating the intra-Gulf domain (see Bonini et al., 2019).

Our observations of oblique slip on graben-bounding faults in our oblique extension models imply that in extensional settings, normal faults that are oblique to the regional extension direction most likely accommodates deformation by both dip- and strike- slip displacements. Although the dip-slip component of such faults may be greater, they are, however, not pure normal faults, but rather oblique normal faults. This is the case in the border faults of the NE-trending rift graben of the Parnaíba Basin, Brazil, which developed as a result of the reactivation of the underlying NE-SW-trending Transbrasiliano Shear Zone under N-S regional extension (Fig. 1c) (see de Castro et al., 2016). Similar minor strike-slip component is reported in several border fault systems that are oblique to the regional extension direction in other natural rift settings, including the Northern Main Ethiopian Rift (e.g., Boccaletti et al., 1998; Corti, 2009), Gulf of Aden (Dauteuil et al., 2001), the Gulf of California (e.g., Withjack & Jamison, 1986; Bonini et al., 2019), and the Mohns Ridge, Norwegian Sea (Dauteuil & Brun, 1996). We note that, in outcrop-based fault analysis, the horizontal offset of markers and kinematic indicators such as slickenlines allows for the discrimination of oblique normal faults from pure normal faults. However, in seismic reflection-based analysis, it is more challenging to constrain the strike-slip component of displacement on normal faults due to the absence of obvious kinematic indicators, and as such only the dip-slip (throw) component is quantified. Therefore, care should be taken when using results of such analysis to scale fault length – displacement relationship, as they may likely skew such relationship more towards under displaced faults.

In contrast to settings where faults that are oblique to the regional extension direction accommodate deformation by both dip- and strike- slip displacements, other natural examples have been observed where faults striking oblique to the regional extension are pure dip-slip (normal) faults, e.g., the Rukwa Rift segment of the East African Rift (Morley, 2010), and Main Ethiopian Rift (Corti et al., 2013). To explain the later, Morley (2010) proposed that the presence of pre-existing weak zones in the brittle crust can result in the local re-orientation of the regional stress field, such that the maximum horizontal stress lies sub-parallel to the weak zone. This explanation has been supported by the interpretation of analogue models by Corti et al. (2013) and Philippon et al. (2015) partly based on re-analysis of earlier analogue models. This contrasting influence of pre-existing weak zones raises an important question of which conditions favor strain partitioning vs. stress re-orientation in extensional settings. Although answering this question is beyond the scope of this current study, we note that Philippon and Corti (2016) suggested that a moderate obliquity threshold of 45° could mark the transition from stress re-orientation to strain partitioning in a divergent setting, while our model results suggests that strain partitioning may already occur at lower obliquity. The difference could lie in the different experimental methods used (centrifuge vs. normal gravity modeling) including the respective boundary conditions and/or material properties. Detailed field as well as high-resolution analogue- and numerical- modeling studies will be key to addressing this question.

5 Conclusions

In this study, we have investigated how the variability in the size, orientation, depth and overall geometry of pre-existing weak zones influence the structural style and pattern of strain localization during rifting. We achieved this through a series of extensional analogue models consisting of weak zone made from silicone oil that is placed inside a layer of quartz sand, mimicking a brittle crust with inherited weak zone. We deployed digital image correlation technique to monitor the progressive surface deformation, allowing the cumulative horizontal displacement to be constrained at a high resolution. Our results have implication for improving the understanding of the role of inherited structures, specifically crustal shear zones on rifts and rift-related faulting. Our key findings may be summarized as follows:

1. The presence of pre-existing weak zones in the brittle crust reduces the integrated strength of the crust that may facilitate strain localization in the vicinity of the weakened crust, resulting in the formation of rift graben. The graben is bounded by new faults whose geometries are influenced by the orientation of the pre-existing weak zones when the weak zone is oriented at $\geq 60^{o}$ to the extension direction. The scale of the weak zone becomes an important factor when it is oriented at a much lower angle ($\leq 45^{o}$) to the extension direction, in which case only large-scale weak zones may effectively weaken the crust and localize strain. Additionally, shallow weak zones are more likely to influence the pattern of deformation in the cover during subsequent rifting compared to deep weak zones. These observations underscore how different properties of a pre-existing weak zone may interplay to control its influence during rifting.
2. The timing of faulting and the amount of strain accommodated by graben-bounding faults are influenced by the orientation, size, or the depth of pre-existing weak zone. Graben-bounding faults nucleate earlier and accommodate more normal strain when the weak zone is: (i) oriented orthogonal to the extension direction compared to oblique orientation, (ii) large-scale compared to small-scale, and (iii) shallow compared to deeply buried.
3. Strain is mainly accommodated by pure dip-slip on normal faults, when the weak zone is orthogonal to the extension direction (i.e., orthogonal rift). Whereas, when the weak zone is oblique to the extension direction (i.e., oblique rift), strain is partitioned (increasing partitioning with increasing obliquity) into: (i) graben-bounding faults characterized by oblique-slip motion (i.e., major dip-slip, with minor component of strike-slip), and (ii) intra-graben domain dominated by strike-slip structures.

4. Under oblique extension, intra-graben faults that are orthogonal to the extension direction, initiates as strike-slip, antithetic Riedel shears.

Acknowledgments, Samples, and Data

This research forms part of the Syn-Rift Systems Project funded by the Research Council of Norway (project number 255229), Aker BP, ConocoPhillips, DNO, Equinor, Neptune and Tullow Oil to the University of Bergen and academic partners the universities of Leeds, East Anglia, Lorraine and the National and Kapodistrian University of Athens. We thank DEEP Research School, Norway, and Erasmus+ for supporting the research stay of Edoseghe at GFZ Potsdam, Germany. Michael Rudolf has been supported by Deutsche Forschungsgemeinschaft (DFG) through grant CRC 1114 "Scaling Cascades in Complex Systems", Project Number 235221301, Project B01. We also thank the Norwegian Academy of Science and Letters for supporting Gawthorpe's VISTA Professorship which also provided a visiting researcher scholarship to Edoseghe. We thank Iverna Creton for laboratory assistance and stimulating discussions. Frank Neumann and Thomas Ziegenhagen are thanked for engineering and technical assistance. We also thank Sebastian Wolf for constructive discussions and suggestions during the preparation of the manuscript. We thank the reviewers Frank Zwaan, two anonymous reviewers, an anonymous associate editor, and Editor Laurent Jolivet for their constructive feedback and suggestions that significantly improved the manuscript. We thank GFZ data services for publishing the data underlying this Study.

All data underlying this study will be available in a GFZ Data Services open access publication (Osagiede et al., 2020b).

References

Aanyu, K., & Koehn, D. (2011). Influence of pre-existing fabrics on fault kinematics and rift geometry of interacting segments: analogue models based on the Albertine Rift (Uganda), Western Branch-East African Rift System. *Journal of African Earth Sciences, 59*(2-3), 168-184.

Ackermann, R. V., & Schlische, R. W. (1997). Anticlustering of small normal faults around larger faults. *Geology, 25*(12), 1127-1130.

Adam, J., Urai, J., Wieneke, B., Oncken, O., Pfeiffer, K., Kukowski, N., Lohrmann, J., Hoth, S., Van Der Zee, W., & Schmatz, J. (2005). Shear localisation and strain distribution during tectonic faulting—New insights from granular-flow experiments and high-resolution optical image correlation techniques. *Journal of Structural Geology, 27*(2), 283-301.

Agostini, A., Bonini, M., Corti, G., Sani, F., & Mazzarini, F. (2011). Fault architecture in the Main Ethiopian Rift and comparison with experimental models: implications for rift evolution and Nubia–Somalia kinematics. *Earth and Planetary Science Letters, 301*(3-4), 479-492.

Agostini, A., Corti, G., Zeoli, A., & Mulugeta, G. (2009). Evolution, pattern, and partitioning of deformation during oblique continental rifting: Inferences from lithospheric-scale centrifuge models. *Geochemistry, Geophysics, Geosystems, 10*(11).

Allemand, P., & Brun, J.-P. (1991). Width of continental rifts and rheological layering of the lithosphere. *Tectonophysics, 188*(1-2), 63-69.

Allken, V., Huismans, R. S., & Thieulot, C. (2012). Factors controlling the mode of rift interaction in brittle-ductile coupled systems: A 3D numerical study. *Geochemistry, Geophysics, Geosystems, 13*(5).

Autin, J., Bellahsen, N., Husson, L., Beslier, M. o., Leroy, S., & d'Acremont, E. (2010). Analog models of oblique rifting in a cold lithosphere. *Tectonics, 29*(6).

Autin, J., Bellahsen, N., Leroy, S., Husson, L., Beslier, M.-O., & d'Acremont, E. (2013). The role of structural inheritance in oblique rifting: Insights from analogue models and application to the Gulf of Aden. *Tectonophysics, 607*, 51-64.

Bahroudi, A., Koyi, H. A., & Talbot, C. J. (2003). Effect of ductile and frictional décollements on style of extension. *Journal of Structural Geology, 25*(9), 1401-1423.

Bartholomew, I., Peters, J., & Powell, C. (1993). *Regional structural evolution of the North Sea: oblique slip and the reactivation of basement lineaments.* Paper presented at the Geological Society, London, Petroleum Geology Conference series.

Basile, C., & Brun, J. P. (1999). Transtensional faulting patterns ranging from pull-apart basins to transform continental margins: an experimental investigation. *Journal of Structural Geology, 21*(1), 23-37.

Bellahsen, N., Daniel, J.-M., Bollinger, L., & Burov, E. (2003). Influence of viscous layers on the growth of normal faults: insights from experimental and numerical models. *Journal of Structural Geology, 25*(9), 1471-1485.

Bellahsen, N., & Daniel, J. M. (2005). Fault reactivation control on normal fault growth: an experimental study. *Journal of Structural Geology, 27*(4), 769-780.

Boccaletti, M., Bonini, M., Mazzuoli, R., Abebe, B., Piccardi, L., & Tortorici, L. (1998). Quaternary oblique extensional tectonics in the Ethiopian Rift (Horn of Africa). *Tectonophysics, 287*(1-4), 97-116.

Bonini, L., Basili, R., Toscani, G., Burrato, P., Seno, S., & Valensise, G. (2015). The role of pre-existing discontinuities in the development of extensional faults: an analog modeling perspective. *Journal of Structural Geology, 74*, 145-158.

Bonini, M., Cerca, M., Moratti, G., López-Martínez, M., Corti, G., & Gracia-Marroquín, D. (2019). Strain partitioning in highly oblique rift settings: Inferences from the southwestern margin of the Gulf of California (Baja California Sur, México). *Tectonics, 38*(12), 4426-4453.

Bonini, M., Souriot, T., Boccaletti, M., & Brun, J. P. (1997). Successive orthogonal and oblique extension episodes in a rift zone: Laboratory experiments with application to the Ethiopian Rift. *Tectonics, 16*(2), 347-362.

Brun, J. P. (1999). Narrow rifts versus wide rifts: inferences for the mechanics of rifting from laboratory experiments. *Philosophical Transactions of the Royal Society of London. Series A: Mathematical, Physical and Engineering Sciences, 357*(1753), 695-712.

Brune, S. (2014). Evolution of stress and fault patterns in oblique rift systems: 3-D numerical lithospheric-scale experiments from rift to breakup. *Geochemistry, Geophysics, Geosystems, 15*(8), 3392-3415.

Brune, S., & Autin, J. (2013). The rift to break-up evolution of the Gulf of Aden: Insights from 3D numerical lithospheric-scale modelling. *Tectonophysics, 607*, 65-79.

Brune, S., Corti, G., & Ranalli, G. (2017). Controls of inherited lithospheric heterogeneity on rift linkage: Numerical and analog models of interaction between the Kenyan and Ethiopian rifts across the Turkana depression. *Tectonics, 36*(9), 1767-1786.

Brune, S., Popov, A. A., & Sobolev, S. V. (2012). Modeling suggests that oblique extension facilitates rifting and continental break-up. *Journal of Geophysical Research: Solid Earth, 117*(B8).

Chattopadhyay, A., & Chakra, M. (2013). Influence of pre-existing pervasive fabrics on fault patterns during orthogonal and oblique rifting: an experimental approach. *Marine and Petroleum Geology, 39*(1), 74-91.

Chemenda, A., Déverchère, J., & Calais, E. (2002). Three-dimensional laboratory modelling of rifting: application to the Baikal Rift, Russia. *Tectonophysics, 356*(4), 253-273.

Claringbould, J. S., Bell, R. E., Jackson, C. A.-L., Gawthorpe, R. L., & Odinsen, T. (2017). Pre-existing normal faults have limited control on the rift geometry of the northern North Sea. *Earth and Planetary Science Letters*, *475*, 190-206.

Clifton, A. E., Schlische, R. W., Withjack, M. O., & Ackermann, R. V. (2000). Influence of rift obliquity on fault-population systematics: results of experimental clay models. *Journal of Structural Geology, 22*(10), 1491-1509.

Collanega, L., Siuda, K., Jackson, C. A. L., Bell, R. E., Coleman, A. J., Lenhart, A., Magee, C., & Breda, A. (2019). Normal fault growth influenced by basement fabrics: the importance of preferential nucleation from pre-existing structures. *Basin Research*, *31*, 659-687. doi:10.1111/bre.12327

Corti, G. (2004). Centrifuge modelling of the influence of crustal fabrics on the development of transfer zones: insights into the mechanics of continental rifting architecture. *Tectonophysics, 384*(1-4), 191-208.

Corti, G. (2008). Control of rift obliquity on the evolution and segmentation of the main Ethiopian rift. *Nature Geoscience, 1*(4), 258-262.

Corti, G. (2009). Continental rift evolution: from rift initiation to incipient break-up in the Main Ethiopian Rift, East Africa. *Earth-Science Reviews, 96*(1-2), 1-53.

Corti, G. (2012). Evolution and characteristics of continental rifting: Analog modeling-inspired view and comparison with examples from the East African Rift System. *Tectonophysics, 522*, 1-33.

Corti, G., Bonini, M., Innocenti, F., Manetti, P., & Mulugeta, G. (2001). Centrifuge models simulating magma emplacement during oblique rifting. *Journal of Geodynamics, 31*(5), 557-576.

Corti, G., Philippon, M., Sani, F., Keir, D., & Kidane, T. (2013). Re-orientation of the extension direction and pure extensional faulting at oblique rift margins: Comparison between the Main Ethiopian Rift and laboratory experiments. *Terra Nova, 25*(5), 396-404.

Corti, G., Van Wijk, J., Bonini, M., Sokoutis, D., Cloetingh, S., Innocenti, F., & Manetti, P. (2003). Transition from continental break-up to punctiform seafloor spreading: How fast, symmetric and magmatic. *Geophysical Research Letters, 30*(12).

Corti, G., van Wijk, J., Cloetingh, S., & Morley, C. K. (2007). Tectonic inheritance and continental rift architecture: Numerical and analogue models of the East African Rift system. *Tectonics, 26*(6), 1-13. doi:10.1029/2006TC002086

Cowie, P. (1998). A healing–reloading feedback control on the growth rate of seismogenic faults. *Journal of Structural Geology, 20*(8), 1075-1087.

Daly, M., Chorowicz, J., & Fairhead, J. (1989). Rift basin evolution in Africa: the influence of reactivated steep basement shear zones. *Geological Society, London, Special Publications, 44*(1), 309-334.

Dauteuil, O., & Brun, J.-P. (1993). Oblique rifting in a slow-spreading ridge. *Nature, 361*(6408), 145-148.

Dauteuil, O., & Brun, J. P. (1996). Deformation partitioning in a slow spreading ridge undergoing oblique extension: Mohns Ridge, Norwegian Sea. *Tectonics, 15*(4), 870-884.

Dauteuil, O., Huchon, P., Quemeneur, F., & Souriot, T. (2001). Propagation of an oblique spreading centre: the western Gulf of Aden. *Tectonophysics, 332*(4), 423-442.

Dautriat, J., Bornert, M., Gland, N., Dimanov, A., & Raphanel, J. (2011). Localized deformation induced by heterogeneities in porous carbonate analysed by multi-scale digital image correlation. *Tectonophysics, 503*(1-2), 100-116.

Dawson, S. M., Laó-Dávila, D. A., Atekwana, E. A., & Abdelsalam, M. G. (2018). The influence of the Precambrian Mughese Shear Zone structures on strain accommodation in the northern Malawi Rift. *Tectonophysics, 722*, 53-68.

de Castro, D., Bezerra, F., Fuck, R., & Vidotti, R. (2016). Geophysical evidence of pre-sag rifting and post-rifting fault reactivation in the Parnaíba basin, Brazil. *Solid Earth*, *7*, 529-548. doi:10.5194/se-7-529-2016

Del Ventisette, C., Bonini, M., Agostini, A., Corti, G., Maestrelli, D., & Montanari, D. (2019). Using different grain-size granular mixtures (quartz and K-feldspar sand) in analogue extensional models. *Journal of Structural Geology*, 103888. doi:https://doi.org/10.1016/j.jsg.2019.103888

Deng, C., Gawthorpe, R. L., Finch, E., & Fossen, H. (2017). Influence of a pre-existing basement weakness on normal fault growth during oblique extension: Insights from discrete element modeling. *Journal of Structural Geology, 105*, 44-61.

Duclaux, G., Huismans, R. S., & May, D. A. (2020). Rotation, narrowing, and preferential reactivation of brittle structures during oblique rifting. *Earth and Planetary Science Letters, 531*, 115952.

Dunbar, J. A., & Sawyer, D. S. (1988). Continental rifting at pre-existing lithospheric weaknesses. *Nature, 333*(6172), 450-452.

Dyksterhuis, S., Rey, P., Müller, R., & Moresi, L. (2007). Effects of initial weakness on rift architecture. *Geological Society, London, Special Publications, 282*(1), 443-455.

Fazlikhani, H., & Back, S. (2015). The influence of pre-existing structure on the growth of syn-sedimentary normal faults in a deltaic setting, Niger Delta. *Journal of Structural Geology, 73*, 18-32. doi:http://dx.doi.org/10.1016/j.jsg.2015.01.011

Fazlikhani, H., Fossen, H., Gawthorpe, R. L., Faleide, J., & Bell, R. E. (2017). Basement structure and its influence on the structural configuration of the northern North Sea.

Ge, Z., Rosenau, M., Warsitzka, M., & Gawthorpe, R. L. (2019). Overprinting translational domains in passive margin salt basins: insights from analogue modelling. *Solid Earth, 10*(4), 1283-1300.

Ghosh, N., Hatui, K., & Chattopadhyay, A. (2020). Evolution of fault patterns within a zone of pre-existing pervasive anisotropy during two successive phases of extensions: an experimental study. *Geo-Marine Letters, 40*(1), 53-74.

Gibson, G. M., Totterdell, J., White, L. T., Mitchell, C., Stacey, A., Morse, M., & Whitaker, A. (2013). Pre-existing basement structure and its influence on continental rifting and fracture zone development along Australia's southern rifted margin. *Journal of the Geological Society, 170*(2), 365-377.

Gupta, A., & Scholz, C. H. (2000). A model of normal fault interaction based on observations and theory. *Journal of Structural Geology, 22*(7), 865-879.

Heilman, E., Kolawole, F., Atekwana, E. A., & Mayle, M. (2019). Controls of Basement Fabric on the Linkage of Rift Segments. *Tectonics, 38*(4), 1337-1366.

Henza, A. A., Withjack, M. O., & Schlische, R. W. (2010). Normal-fault development during two phases of non-coaxial extension: An experimental study. *Journal of Structural Geology, 32*(11), 1656-1667.

Hubbert, M. K. (1937). Theory of scale models as applied to the study of geologic structures. *Geological Society of America Bulletin, 48*(10), 1459-1520.

Keep, M., & McClay, K. (1997). Analogue modelling of multiphase rift systems. *Tectonophysics, 273*(3), 239-270.

Kirkpatrick, J., Bezerra, F., Shipton, Z., Do Nascimento, A., Pytharouli, S., Lunn, R., & Soden, A. (2013). Scale-dependent influence of pre-existing basement shear zones on rift faulting: a case study from NE Brazil. *Journal of the Geological Society, 170*(2), 237-247.

Klinkmüller, M., Schreurs, G., Rosenau, M., & Kemnitz, H. (2016). Properties of granular analogue model materials: A community wide survey. *Tectonophysics, 684*, 23-38.

Kolawole, F., Atekwana, E. A., Laó-Dávila, D. A., Abdelsalam, M. G., Chindandali, P. R., Salima, J., & Kalindekafe, L. (2018). Active deformation of Malawi rift's north basin Hinge zone modulated by reactivation of preexisting Precambrian Shear zone fabric. *Tectonics, 37*(3), 683-704.

Le Calvez, J. H., & Vendeville, B. C. (2002). Physical modeling of normal faults and graben relays above salt: A qualitative and quantitative analysis. *Gulf Coast Association of Geological Societies Transactions, 52*, 599 - 606.

Lohrmann, J., Kukowski, N., Adam, J., & Oncken, O. (2003). The impact of analogue material properties on the geometry, kinematics, and dynamics of convergent sand wedges. *Journal of Structural Geology, 25*(10), 1691-1711.

Maerten, L., Gillespie, P., & Pollard, D. D. (2002). Effects of local stress perturbation on secondary fault development. *Journal of Structural Geology, 24*(1), 145-153.

Maestrelli, D., Montanari, D., Corti, G., Del Ventisette, C., Moratti, G., & Bonini, M. (2020). Exploring the Interactions Between Rift Propagation and Inherited Crustal Fabrics Through Experimental Modeling. *Tectonics, 39*(12), e2020TC006211.

Maniatis, G., & Hampel, A. (2008). Along-strike variations of the slip direction on normal faults: Insights from three-dimensional finite-element models. *Journal of Structural Geology, 30*(1), 21-28.

Maurin, J.-C., & Guiraud, R. (1993). Basement control in the development of the Early Cretaceous West and Central African rift system. *Tectonophysics, 228*(1-2), 81-95.

McClay, K., Dooley, T., Whitehouse, P., & Mills, M. (2002). 4-D evolution of rift systems: Insights from scaled physical models. *AAPG Bulletin, 86*(6), 935-959.

McClay, K., & White, M. (1995). Analogue modelling of orthogonal and oblique rifting. *Marine and Petroleum Geology, 12*(2), 137-151.

McConnell, R. B. (1967). The east African rift system. *Nature, 215*(5101), 578-581.

Michon, L., & Merle, O. (2000). Crustal structures of the Rhinegraben and the Massif Central grabens: An experimental approach. *Tectonics, 19*(5), 896-904.

Michon, L., & Sokoutis, D. (2005). Interaction between structural inheritance and extension direction during graben and depocentre formation: An experimental approach. *Tectonophysics, 409*(1-4), 125-146.

Molnar, N., Cruden, A., & Betts, P. (2020). The role of inherited crustal and lithospheric architecture during the evolution of the Red Sea: Insights from three dimensional analogue experiments. *Earth and Planetary Science Letters, 544*, 116377.

Molnar, N. E., Cruden, A. R., & Betts, P. G. (2019). Interactions between propagating rifts and linear weaknesses in the lower crust. *Geosphere, 15*(5), 1617-1640.

Morley, C. (1995). Developments in the structural geology of rifts over the last decade and their impact on hydrocarbon exploration. *Geological Society, London, Special Publications, 80*(1), 1-32.

Morley, C. (2010). Stress re-orientation along zones of weak fabrics in rifts: An explanation for pure extension in 'oblique'rift segments? *Earth and Planetary Science Letters, 297*(3-4), 667-673.

Morley, C., Haranya, C., Phoosongsee, W., Pongwapee, S., Kornsawan, A., & Wonganan, N. (2004). Activation of rift oblique and rift parallel pre-existing fabrics during extension and their effect on deformation style: examples from the rifts of Thailand. *Journal of Structural Geology, 26*(10), 1803-1829.

Muirhead, J., & Kattenhorn, S. (2018). Activation of preexisting transverse structures in an evolving magmatic rift in East Africa. *Journal of Structural Geology, 106*, 1-18.

Mulugeta, G. (1988). Squeeze box in a centrifuge. *Tectonophysics, 148*(3-4), 323-335.

Osagiede, E. E., Rosenau, M., Rudolf, M., Rotevatn, A., Gawthorpe, R., & Jackson, C. A.-L. (2020b). Digital image correlation data from analogue modelling experiments addressing extension of weakened crust. *GFZ Data Services*. doi:http://doi.org/10.5880/GFZ.4.1.2020.005

Osagiede, E. E., Rotevatn, A., Gawthorpe, R., Kristensen, T. B., Jackson, C. A., & Marsh, N. (2020a). Pre-existing intra-basement shear zones influence growth and geometry of non-colinear normal faults, western Utsira High–Heimdal Terrace, North Sea. *Journal of Structural Geology, 130*, 103908.

Panien, M., Schreurs, G., & Pfiffner, A. (2006). Mechanical behaviour of granular materials used in analogue modelling: insights from grain characterisation, ring-shear tests and analogue experiments. *Journal of Structural Geology, 28*(9), 1710-1724.

Peacock, D., Nixon, C., Rotevatn, A., Sanderson, D., & Zuluaga, L. (2016). Glossary of fault and other fracture networks. *Journal of Structural Geology, 92*, 12-29.

Philippon, M., & Corti, G. (2016). Obliquity along plate boundaries. *Tectonophysics, 693*, 171-182.

Philippon, M., Willingshofer, E., Sokoutis, D., Corti, G., Sani, F., Bonini, M., & Cloetingh, S. (2015). Slip re-orientation in oblique rifts. *Geology, 43*(2), 147-150.

Phillips, T. B., Fazlikhani, H., Gawthorpe, R. L., Fossen, H., Jackson, C. A. L., Bell, R. E., Faleide, J. I., & Rotevatn, A. (2019). The Influence of Structural Inheritance and Multiphase Extension on Rift Development, the NorthernNorth Sea. *Tectonics*.

Phillips, T. B., Jackson, C. A. L., Bell, R. E., Duffy, O. B., & Fossen, H. (2016). Reactivation of intrabasement structures during rifting: A case study from offshore southern Norway. *Journal of Structural Geology, 91*, 54-73. doi:http://dx.doi.org/10.1016/j.jsg.2016.08.008

Ramberg, H. (1981). *Gravity, deformation and the earth's crust: in theory, experiments and geological application*: Academic press.

Ranalli, G., & Yin, Z.-M. (1990). Critical stress difference and orientation of faults in rocks with strength anisotropies: the two-dimensional case. *Journal of Structural Geology, 12*(8), 1067-1071.

Reeve, M. T., Bell, R. E., Duffy, O. B., Jackson, C. A. L., & Sansom, E. (2015). The growth of non-colinear normal fault systems; What can we learn from 3D seismic reflection data? *Journal of Structural Geology, 70*, 141-155. doi:http://dx.doi.org/10.1016/j.jsg.2014.11.007

Reeve, M. T., Bell, R. E., & Jackson, C. A.-L. (2013). Origin and significance of intra-basement seismic reflections offshore western Norway. *Journal of the Geological Society, 171*(1), 1-4.

Ring, U. (1994). The influence of preexisting structure on the evolution of the Cenozoic Malawi rift (East African rift system). *Tectonics, 13*(2), 313-326.

Ritter, M. C., Leever, K., Rosenau, M., & Oncken, O. (2016). Scaling the sandbox—Mechanical (dis) similarities of granular materials and brittle rock. *Journal of Geophysical Research: Solid Earth, 121*(9), 6863-6879.

Rosenau, M., Pohlenz, A., Kemnitz, H., & Warsitzka, M. (2018). Ring-shear test data of quartz sand G12 used for analogue experiments in the Helmholtz Laboratory for Tectonic Modelling (HelTec) at the GFZ German Research Centre for Geosciences in Potsdam. *GFZ Data Services*. doi:http://doi.org/10.5880/GFZ.4.1.2019.003

Rotevatn, A., Kristensen, T., Ksienzyk, A., Wemmer, K., Henstra, G., Midtkandal, I., Grundvåg, S. A., & Andresen, A. (2018). Structural inheritance and rapid rift-length establishment in a multiphase rift: the East Greenland rift system and its Caledonian orogenic ancestry. *Tectonics, 37*, 1858-1875.

Rudolf, M., Boutelier, D., Rosenau, M., Schreurs, G., & Oncken, O. (2016). Rheological benchmark of silicone oils used for analog modeling of short-and long-term lithospheric deformation. *Tectonophysics, 684*, 12-22.

Salomon, E., Koehn, D., & Passchier, C. (2015). Brittle reactivation of ductile shear zones in NW Namibia in relation to South Atlantic rifting. *Tectonics, 34*(1), 70-85.

Sani, F., Bonini, M., Corti, G., & Moratti, G. (2019). Extension direction re-orientation in the oceanic rift of Iceland, and comparison with continental rifts. *Tectonophysics, 756*, 25-42.

Saria, E., Calais, E., Stamps, D., Delvaux, D., & Hartnady, C. (2014). Present-day kinematics of the East African Rift. *Journal of Geophysical Research: Solid Earth, 119*(4), 3584-3600.

Schellart, W. (2000). Shear test results for cohesion and friction coefficients for different granular materials: scaling implications for their usage in analogue modelling. *Tectonophysics, 324*(1-2), 1-16.

Schellart, W. P., & Strak, V. (2016). A review of analogue modelling of geodynamic processes: Approaches, scaling, materials and quantification, with an application to subduction experiments. *Journal of Geodynamics, 100*, 7-32.

Schlagenhauf, A., Manighetti, I., Malavieille, J., & Dominguez, S. (2008). Incremental growth of normal faults: Insights from a laser-equipped analog experiment. *Earth and Planetary Science Letters, 273*(3-4), 299-311.

Scholz, C. H., & Contreras, J. C. (1998). Mechanics of continental rift architecture. *Geology, 26*(11), 967-970.

Schreurs, G., Buiter, S. J., Boutelier, D., Corti, G., Costa, E., Cruden, A. R., Daniel, J., Hoth, S., Koyi, H. A., & Kukowski, N. (2006). Analogue benchmarks of shortening and extension experiments. *Special Publication-Geological Society Of London, 253*, 1.

Schreurs, G., Buiter, S. J., Boutelier, J., Burberry, C., Callot, J.-P., Cavozzi, C., Cerca, M., Chen, J.-H., Cristallini, E., & Cruden, A. R. (2016). Benchmarking analogue models of brittle thrust wedges. *Journal of Structural Geology, 92*, 116-139.

Sokoutis, D., Corti, G., Bonini, M., Brun, J. P., Cloetingh, S., Mauduit, T., & Manetti, P. (2007). Modelling the extension of heterogeneous hot lithosphere. *Tectonophysics*, *444*(1-4), 63-79.

Soliva, R., Benedicto, A., & Maerten, L. (2006). Spacing and linkage of confined normal faults: importance of mechanical thickness. *Journal of Geophysical Research: Solid Earth, 111*(B1).

Sylvester, A. G. (1988). Strike-slip faults. *Geological Society of America Bulletin, 100*(11), 1666-1703.

Theunissen, K., Klerkx, J., Melnikov, A., & Mruma, A. (1996). Mechanisms of inheritance of rift faulting in the western branch of the East African Rift, Tanzania. *Tectonics*, *15*(4), 776-790.

Tong, H., Koyi, H., Huang, S., & Zhao, H. (2014). The effect of multiple pre-existing weaknesses on formation and evolution of faults in extended sandbox models. *Tectonophysics, 626*, 197-212.

Tron, V., & Brun, J.-P. (1991). Experiments on oblique rifting in brittle-ductile systems. *Tectonophysics, 188*(1-2), 71-84.

Van Wijk, J. (2005). Role of weak zone orientation in continental lithosphere extension. *Geophysical Research Letters*, *32*(2).

Vauchez, A., Tommasi, A., & Barruol, G. (1998). Rheological heterogeneity, mechanical anisotropy and deformation of the continental lithosphere. *Tectonophysics*, *296*(1-2), 61-86.

Versfelt, J., & Rosendahl, B. R. (1989). Relationships between pre-rift structure and rift architecture in Lakes Tanganyika and Malawi, East Africa. *Nature*, *337*(6205), 354-357.

White, D. J., Take, W., & Bolton, M. (2001). Measuring soil deformation in geotechnical models using digital images and PIV analysis. *In 10th International Conference on Computer Methods and Advances in Geomechanics, Tuscon, Arizona*(1), 997-1002.

Withjack, M. O., & Jamison, W. R. (1986). Deformation produced by oblique rifting. *Tectonophysics, 126*(2-4), 99-124.

Wrona, T., Fossen, H., Lecomte, I., Eide, C., & Gawthorpe, R. (2020). Seismic expression of shear zones: Insights from 2-D point-spread-function-based convolution modelling. *Journal of Structural Geology*, 104121.

Zwaan, F., Chenin, P., Erratt, D., Manatschal, G., & Schreurs, G. (in review). Complex rift patterns, a result of interacting crustal and mantle weaknesses, or multiphase rifting? Insights from analogue models. *Solid Earth Discussion (preprint)*, 1-38. doi:https://doi.org/10.5194/se-2020-214

Zwaan, F., & Schreurs, G. (2017). How oblique extension and structural inheritance influence rift segment interaction: Insights from 4D analog models. *Interpretation, 5*(1), SD119-SD138.

Zwaan, F., Schreurs, G., & Buiter, S. (2019). A systematic comparison of experimental set-ups for modelling extensional tectonics. *Solid Earth (SE), 10*(4), 1063-1097.

Zwaan, F., Schreurs, G., Naliboff, J., & Buiter, S. J. (2016). Insights into the effects of oblique extension on continental rift interaction from 3D analogue and numerical models. *Tectonophysics, 693*, 239-260.

Zwaan, F., Schreurs, G., & Rosenau, M. (2020). Rift propagation in rotational versus orthogonal extension: Insights from 4D analogue models. *Journal of Structural Geology, 135*, 103946.

Appendix

Appendix 1

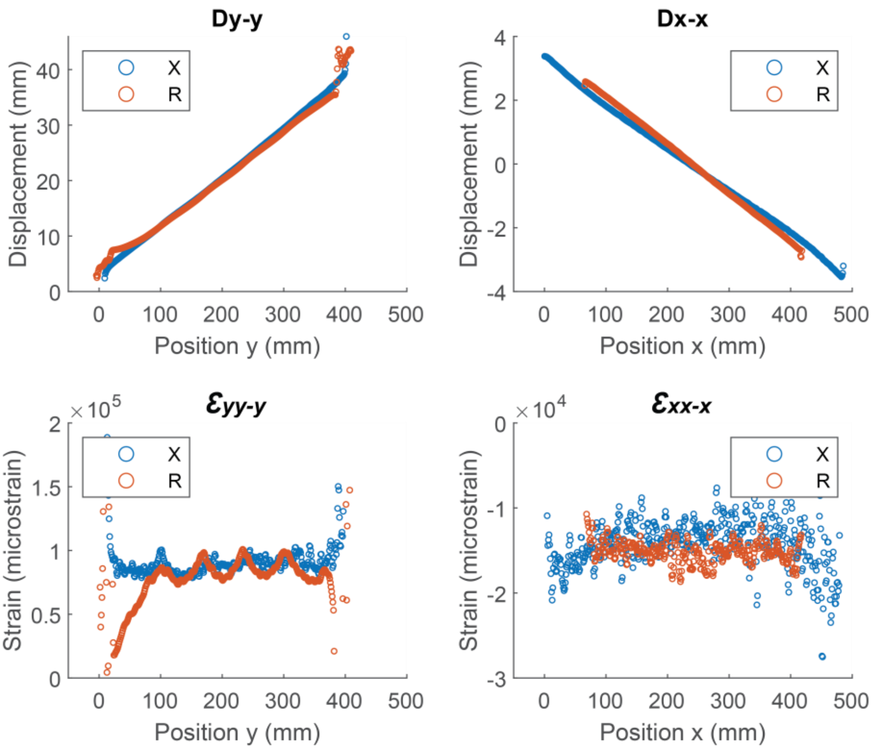

Benchmarks verifying the basal boundary condition of distributed, non-plane strain pure shear: The upper row shows final displacements after 50 mm of externally applied wall motion both parallel (y, left) and normal (x, right) to the extension direction for the benchmark model X (basal foam only) and reference model R (sand layer 40 mm thick). Displacement profiles are linear and parallel suggesting first-order quantitative transfer of homogenous deformation from the basal foam to the sand layer. Middle row shows the corresponding longitudinal strains Eyy-y and Exx-y. Note that strain localization is unavoidable at the boundaries but the central area of interest is homogenously extended longitudinally by c. 8-10 % and shortened transversally by c. 1.5 % resulting in a "Poisson rate" of c. 16%.

Appendix 2

<u>Calculation of strain from vector field and strain rate:</u>

The strain fields for normal strain ε_n and shear strain ε_s are calculated by LaVision DaVis as the gradient in the vector field V_i with respect to the direction j, according to the strain tensor (DaVis 10.1 Manual, 2019):

$\varepsilon_{ij} = \partial V_i / \partial j$ with $i \in \{x, y\}$ and $j \in \{x, y\}$

The normal strain is the gradient in V_y along the y axis $\varepsilon_n = \varepsilon_{yy}$ and therefore representative of compression or extension along the main deformation axis. The shear strain is the change in V_y along the x axis $\varepsilon_s = \varepsilon_{xy}$and represents horizontal shear. Because the vector field is on a discrete grid the strain tensor at a point (n, m) (where n is the matrix index in x and m in y direction) is approximated by taking the average between the neighbouring vectors $V_y(n, m+1)$ and $V_y(n, m-1)$ in the respective direction and multiplying it with the vector spacing d:

$$\varepsilon_{xy}(n, m) = \frac{V_x(n, m+1) - V_x(n, m+1)}{2} \cdot d$$

At the edges of the vector field where one of the neighbouring points does not exist, the missing neighbour is replaced by the value at (n, m). If neither exist, the strain is set to zero. To convert strain ε into strain rates $\dot{\varepsilon}$ the values are multiplied by the time between images Δt:

$$\dot{\varepsilon} = \varepsilon \cdot \Delta t$$

Appendix 3

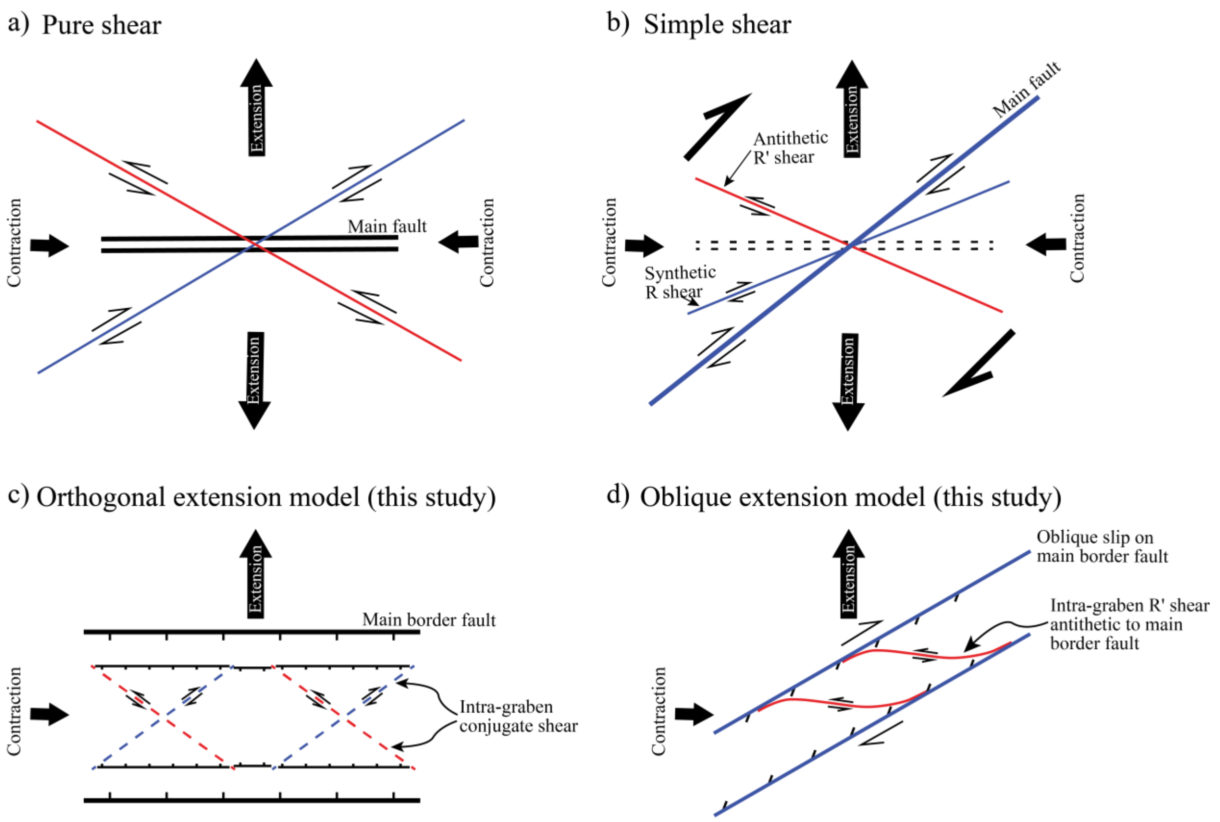

Geometrical relationship of structures associated with pure shear and simple shear kinematics, and how they correlate with the major structures observed in our orthogonal and oblique models based on longitudinal and shear strain analysis (modified from Sylvester, 1988).

Appendix 4

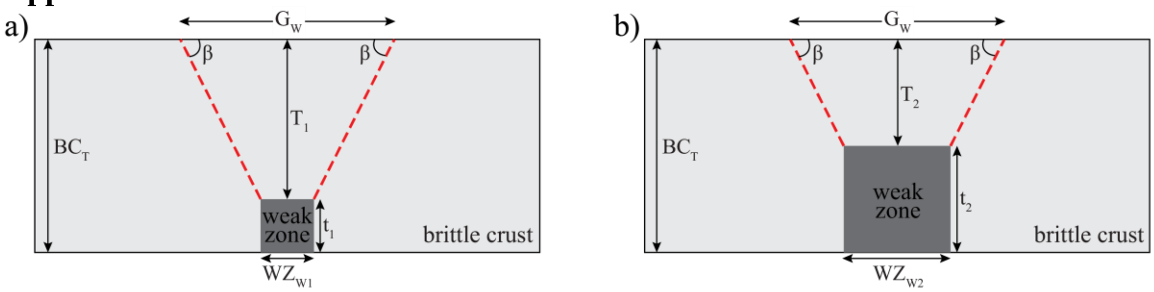

$$\mathbf{G_W = WZ_{W1} + 2(T_1\ cot\beta)}$$

$$\mathbf{G_W = WZ_{W2} + 2(T_2\ cot\beta)}$$

Geometrical relationship between graben width (G_W), the weak zone width (WZ_W), the thickness of the brittle layer above the weak zone (T), and the dip of the graben-bounding faults (β). The graben width is theoretically equal in (a) the small weak zone model and (b) the large weak zone model since the dip of the graben-bounding faults is the same. Modified from Corti (2004).

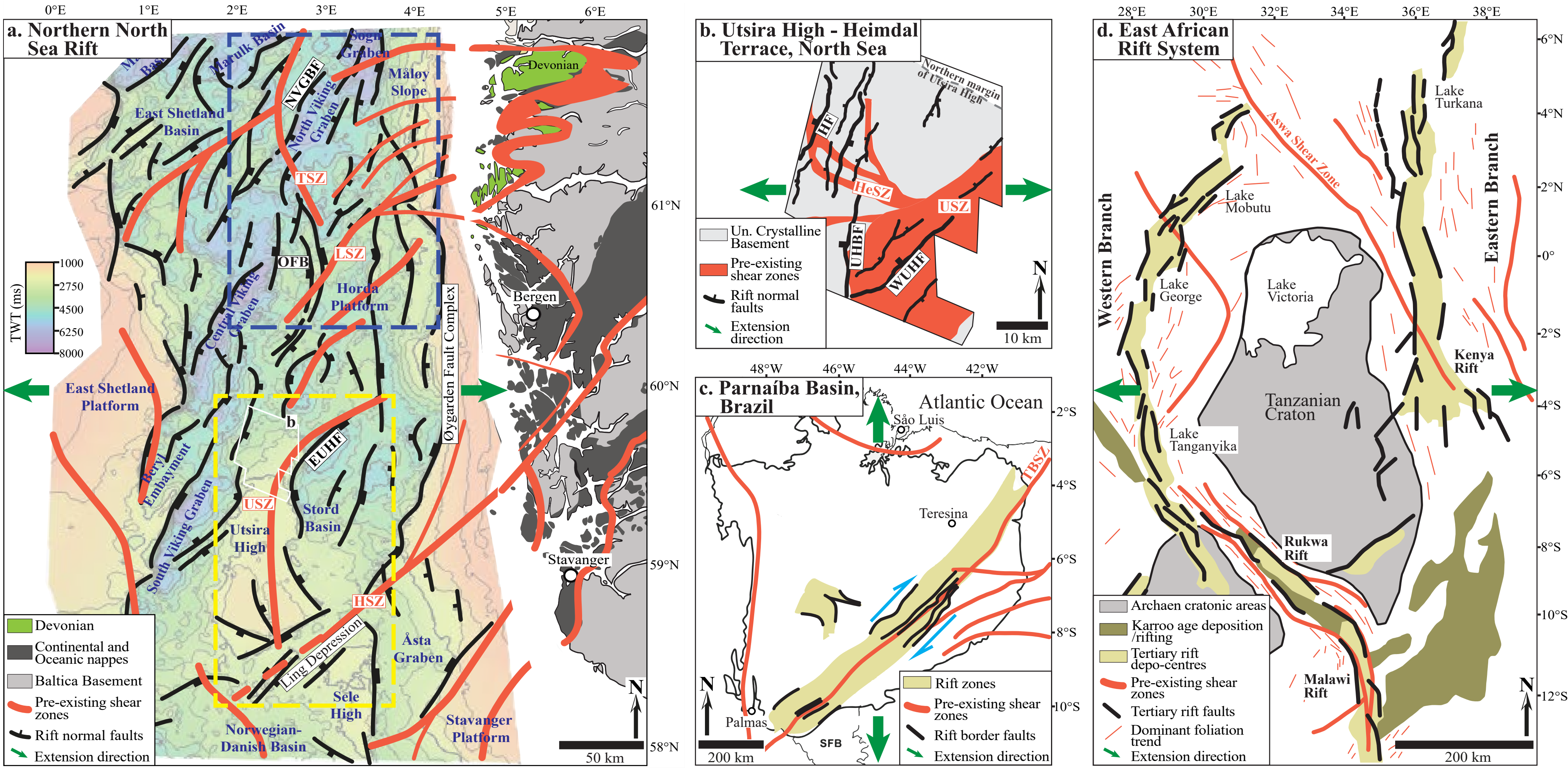

Figure 1: Simplified maps of natural rift systems showing the plan-view relationship between pre-existing shear zones and younger rift-related normal faults/graben structure across a range of scales. (a) Rift-scale: the northern North Sea Rift superimposed on a two-way-time (TWT) structure map at the base rift phase 1 structural level, showing; (i)area marked by the yellow stippled box, where younger rift-related faults and intra-rift graben mimic the plan-view geometry of the underlying pre-existing shear zones (e.g., the Eastern Utsira High Fault, EUHF and the Utsira Shear Zone, USZ; the Ling Depression and the Hardangerfjord Shear Zone, HSZ), and (ii) area marked by the blue stippled box, where younger rift-related faults are oblique to the underlying pre-existing shear zones (e.g., the Oseberg Fault Block, OFB and the Lomre Shear Zone, LSZ; the North Viking Graben Border Fault, NVGBF and the Tampen Shear Zone, TSZ) (modified from Phillips et al., 2019). (b) Fault array-scale: the Utsira High – Heimdal Terrace (see location in Fig. a) showing strong geometric correlation between the Western Utsira High Fault (WUHF) and the pre-existing Utsira Shear Zone, and obliqueness of the Utsira High Border Fault (UHBF) and Heimdal Fault (HF) with the pre-existing Heimdal Shear Zone (HeSZ) (modified from Osagiede et al., 2020a). (c) Basin-scale: the Parnaíba Basin, Brazil showing the correlation of the Parnaíba rift zone with the Transbrasiliano Shear Zone (TBSZ) (modified from de Castro et al., 2016). (d) Rift-scale: the East African Rift System showing the correlation between the Rukwa – Malawi rift segments and the inter-cratonic mobile belt (modified from Morley, 1995).

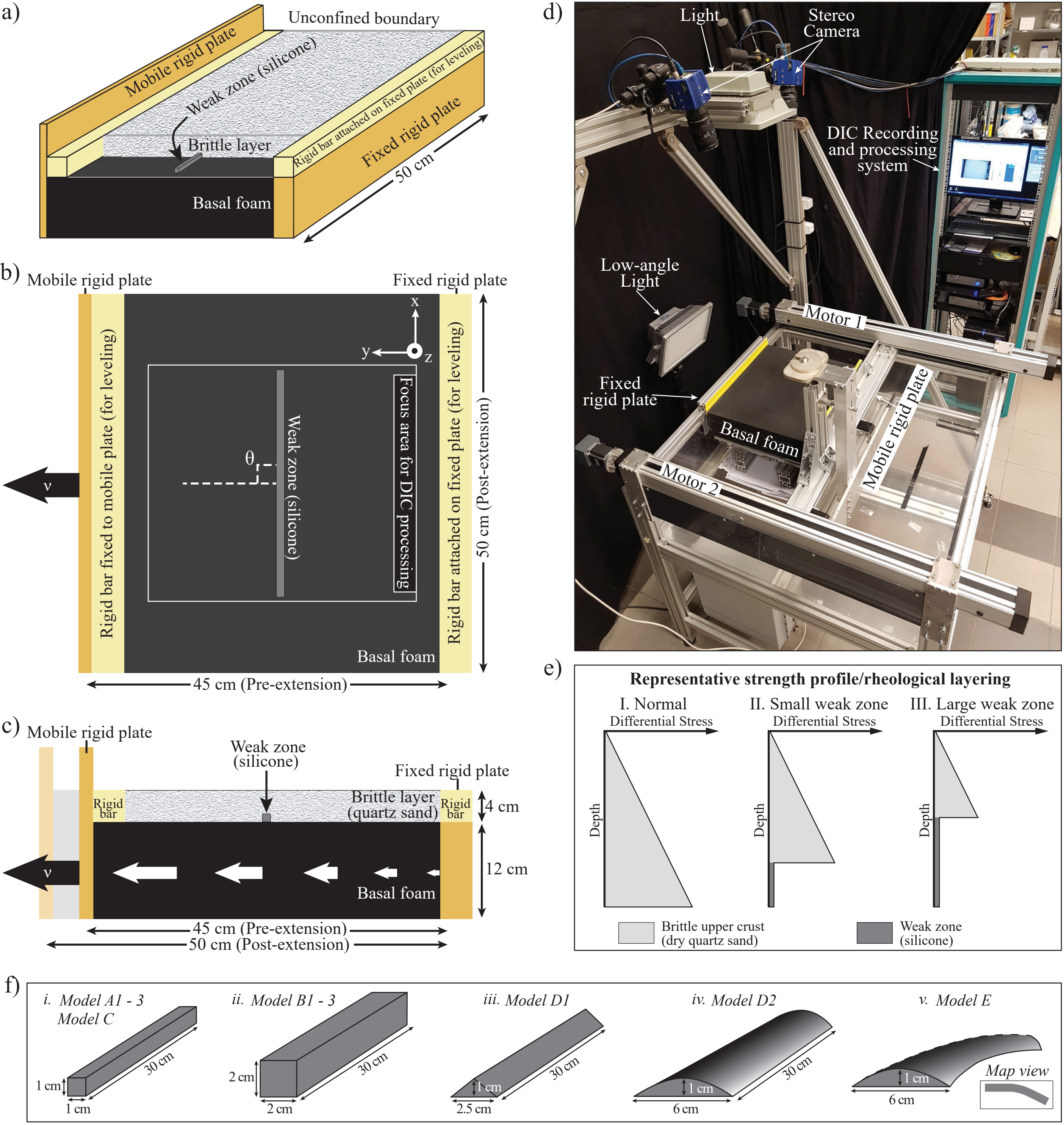

Figure 2: Model setup and apparatus. (a) 3D oblique view indicating the main components of our models. (b) Representative plan-view sketch of our weak zone geometry oriented at θ = 90o to the extension direction represented by the black arrow, and the focus area used for the time-series DIC processing. (c) Representative cross-sectional view, indicating our model layering and distributed deformation at the base of the models. (d) Experimental deformation rig-, recording-, and processing- setups. (e) Hypothetical rheological layering and associated strength profile for the normal (pristine)- and weakened- crust respectively, in our experimental series A (not drawn to scale). (f) The 3D geometry and dimensions of the weak zone used in the different models to simulate a range of natural weak zone geometries (note the map view insert of the weak zone in Model E).

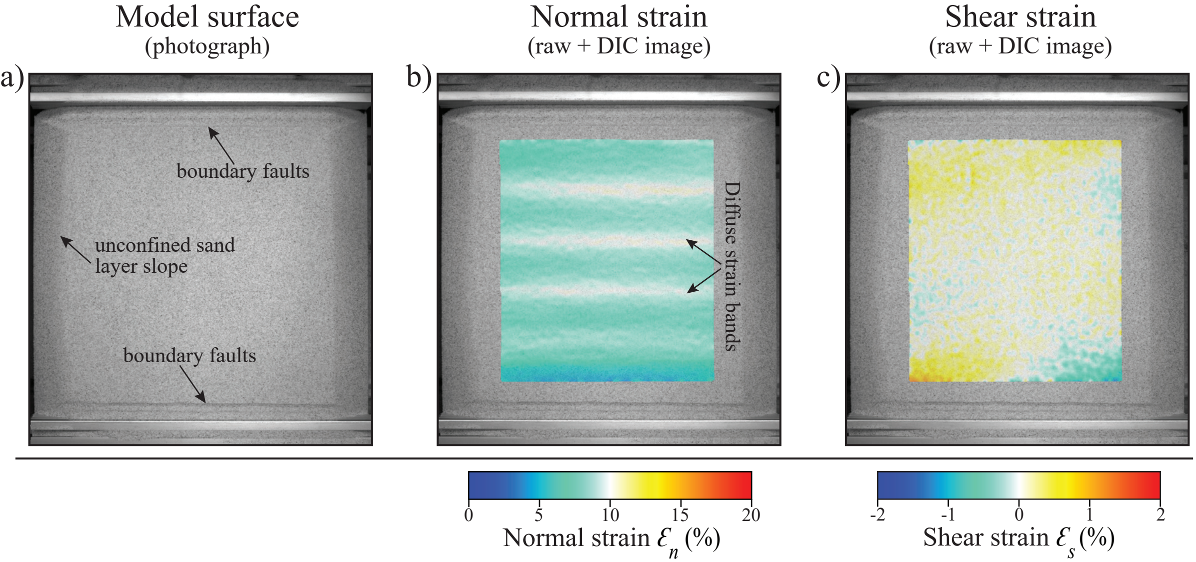

Figure 3: Reference model R consisting of a 4 cm brittle-layer above a basal foam. (a) post-extension image of the model surface characterized by boundary faults that mark 'edge effect'. (b) DIC-derived normal strain component of the model centre (focus area) superimposed on the raw image. There is no strain localization except for the formation of 'diffuse strain bands' (see text for detail). (c) DIC-derived shear strain component of the model centre (focus area) superimposed on the raw image. Shear strain values are c. zero and chaotic.

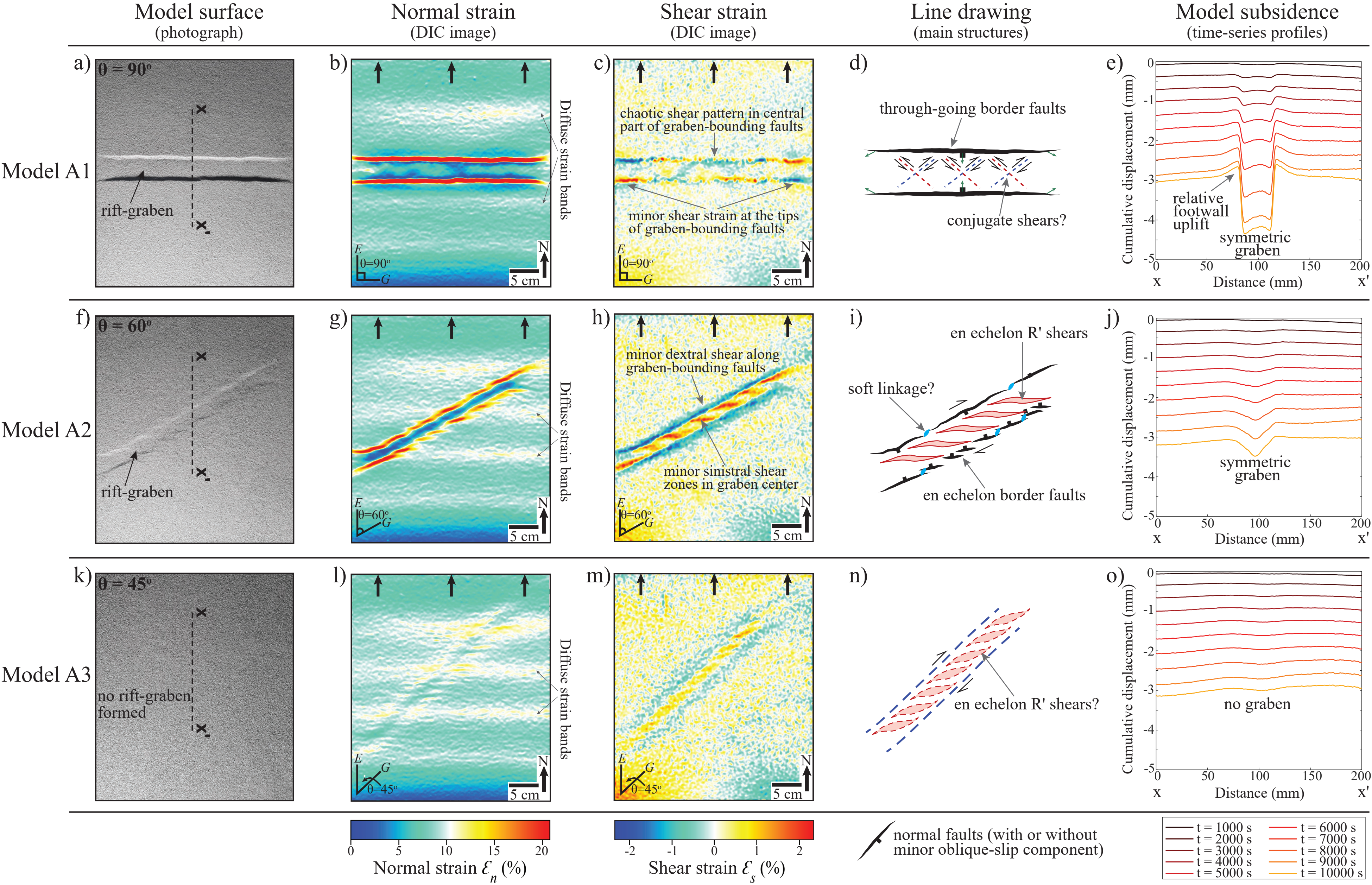

Figure 4: Final stage surface deformation of Experimental Series A (small weak zone); Model A1 (θ = 90°), Model A2 (θ = 60°), Model A3 (θ = 45°). Panel consist of photograph of the central portion of model surface, corresponding DIC-derived normal and shear strain components, line drawing of the main normal and shear structures, and time-series model subsidence profiles. Locations of the subsidence profiles are indicated in the photographs (X - X'). The main structures are annotated and lateral exaggeration on the line drawings is 2x. E = extension direction, G = graben axis, t = time in seconds. Note that an apparent 'northern' direction is imposed for the purpose of description.

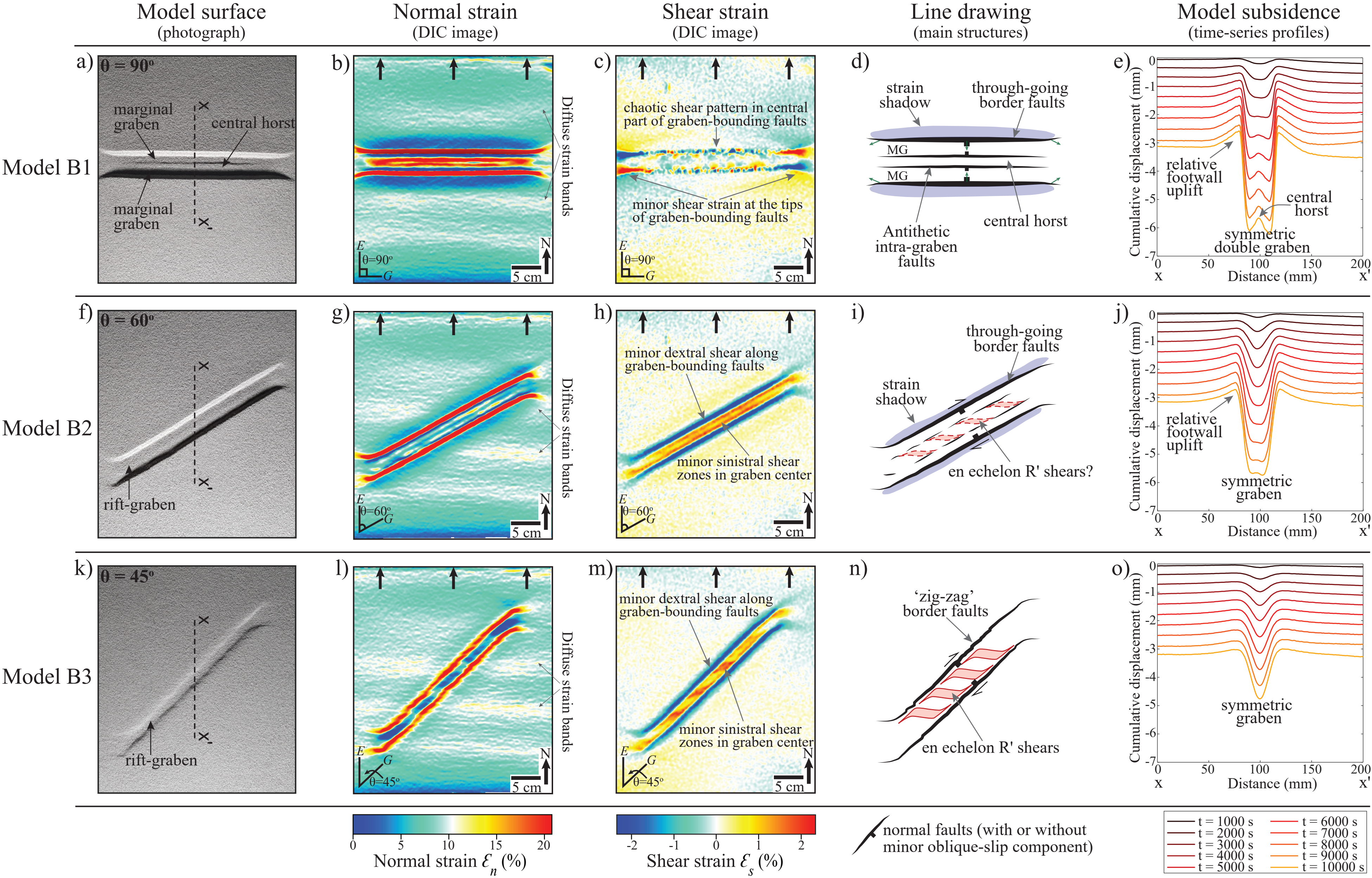

Figure 5: Final stage surface deformation of Experimental Series B (large weak zone); Model B1 (θ = 90°), Model B2 (θ = 60°), Model B3 (θ = 45°). Panel consist of photograph of the central portion of model surface, corresponding DIC-derived normal and shear strain components, line drawing of the main normal and shear structures, and time-series model subsidence profiles. Locations of the subsidence profiles are indicated in the photographs (X - X'). The main structures are annotated and lateral exaggeration on the line drawings is 2x. E = extension direction, G = graben axis, t = time in seconds. Note that an apparent 'northern' direction is imposed for the purpose of description.

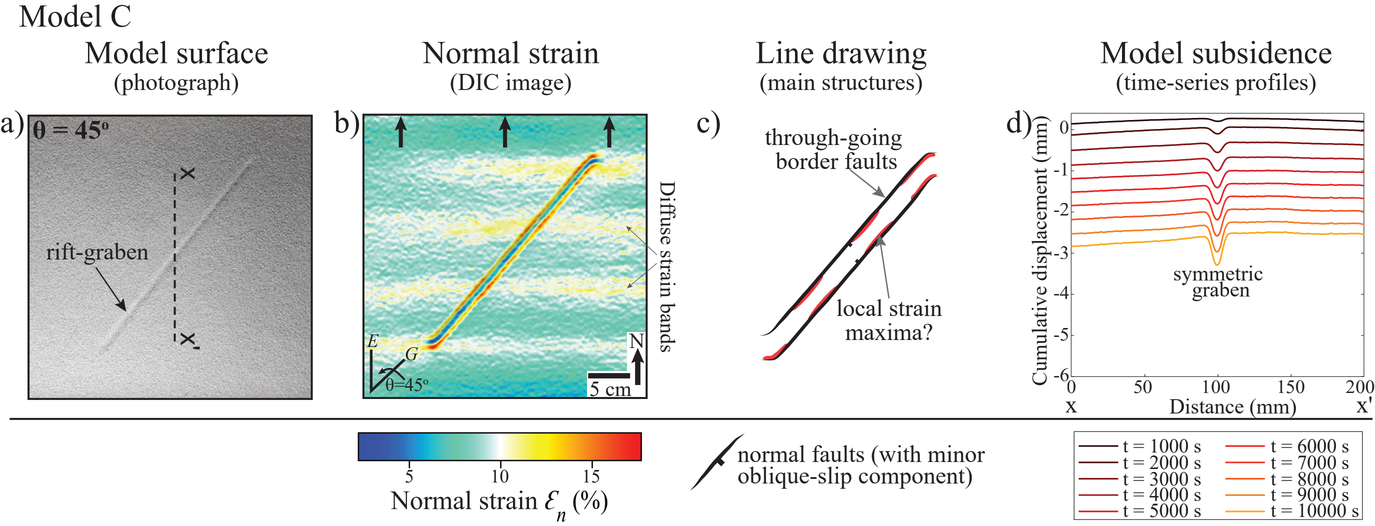

Figure 6: Final stage surface deformation of Experimental Series C (thin brittle layer as proxy for shallow weak zone burial); Model C (θ = 45°). Panels consist of (a) photograph of the central portion of model surface, (b) corresponding DIC-derived normal strain component, (c) line drawing of the main structures, and (d) time-series model subsidence profiles. Location of the subsidence profiles in (d) is indicated in (a). The main structures are annotated and lateral exaggeration on the line drawing is 2x. E = extension direction, G = graben axis, t = time in seconds. Note that an apparent 'northern' direction is imposed for the purpose of description.

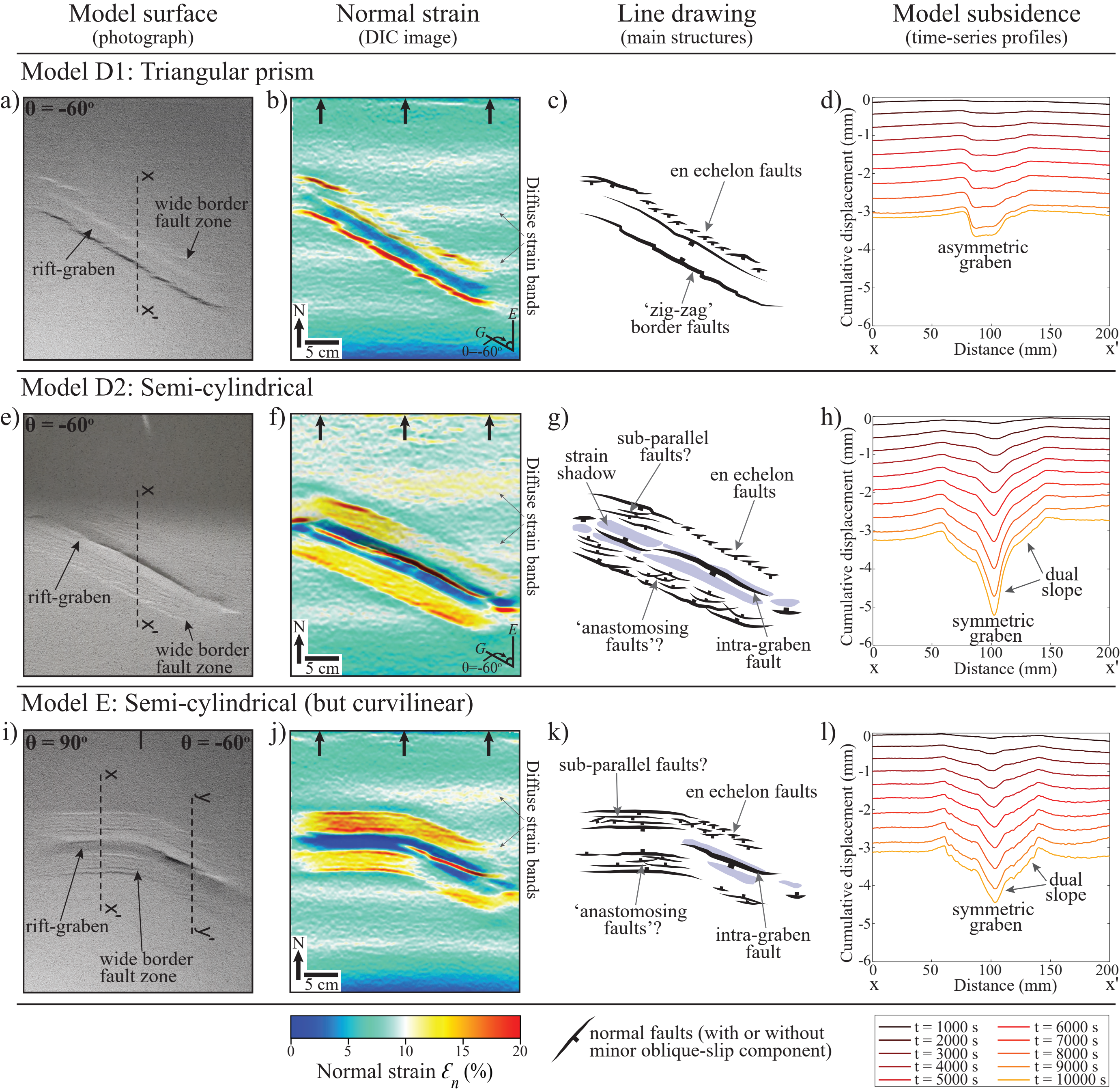

Figure 7: Final stage surface deformation of Experimental Series D and E (variable weak zone geometry); Model D1 (θ = -60°), Model D2 (θ = -60°), Model E (θ = 90° and -60°). Panels consist of photograph of the central portion of model surface, corresponding DIC-derived normal strain components, line drawing of the main structures, and time-series model subsidence profiles. Locations of the subsidence profiles are indicated in the photographs (X - X'). The main structures are annotated. E = extension direction, G = graben axis, t = time in seconds. Note that an apparent 'northern' direction is imposed for the purpose of description.

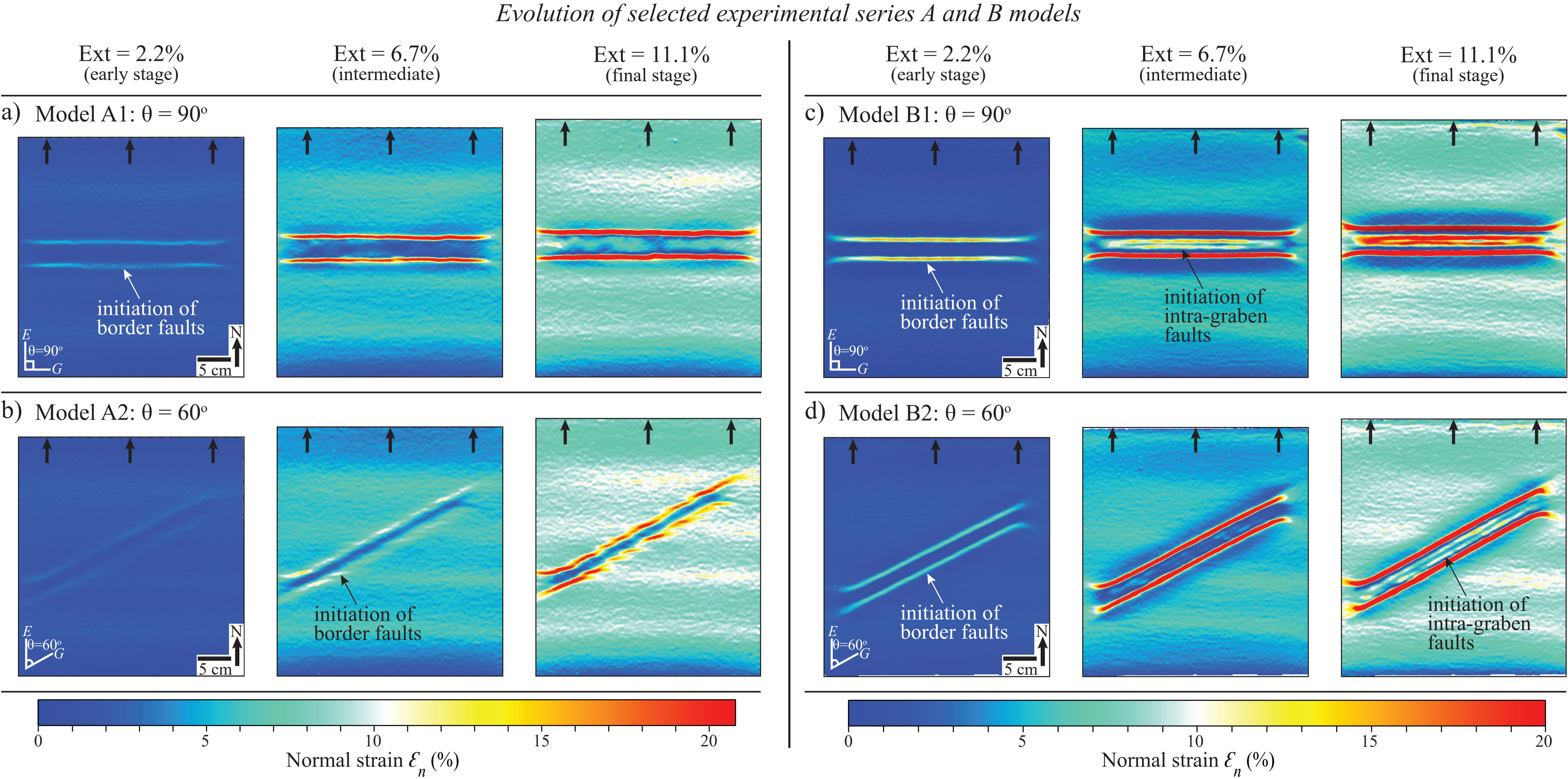

Figure 8: Normal strain distribution based on time-series DIC analysis of selected Experimental Series A (small weak zone) and B (large weak zone) models, corresponding to early stage (2.2% extension), intermediate stage (6.7% extension), and final stage (11.1% extension) deformations. (a) Model A1, θ = 90°. (b) Model A2, θ = 60°. (c) Model B1, θ = 90°. (d) Model B1, θ = 60o. Note the differences in the timing of initiation and relative amount of strain on the main structures as a function of the orientation and size of the weak zone. E = extension direction, G = graben axis. Note that an apparent 'northern' direction is imposed for the purpose of description.

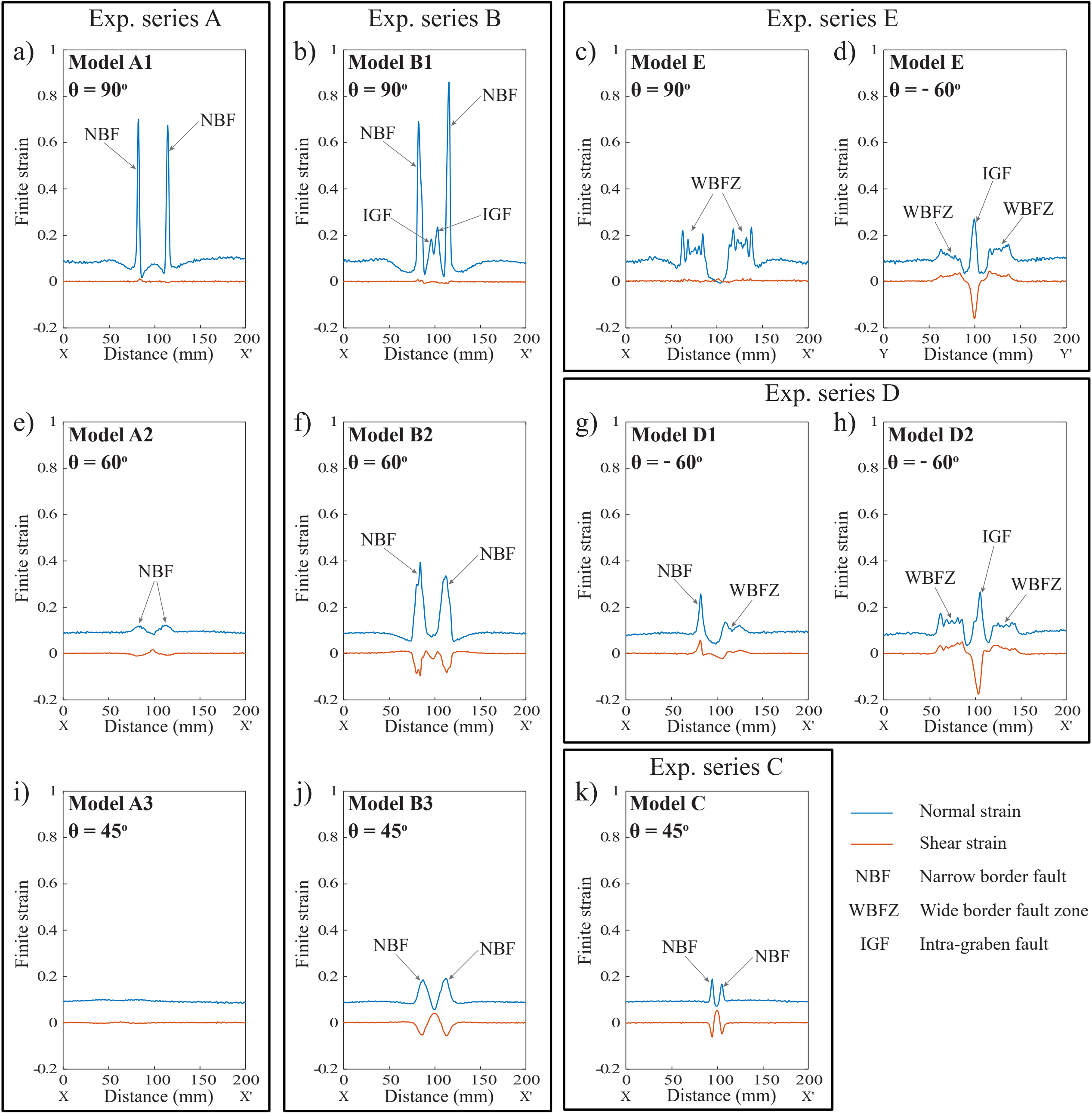

Figure 9: Plot of the final stage normal and shear strain components along profile lines that are parallel to the extension direction, and across the main rift structures in all the experimental series. Note that the normal strain is positive indicating extension, whereas the shear strain is either negative (if dextral) or positive (if sinistral). The locations of the profile lines are indicated in Figs. 4,5,6, and 7.

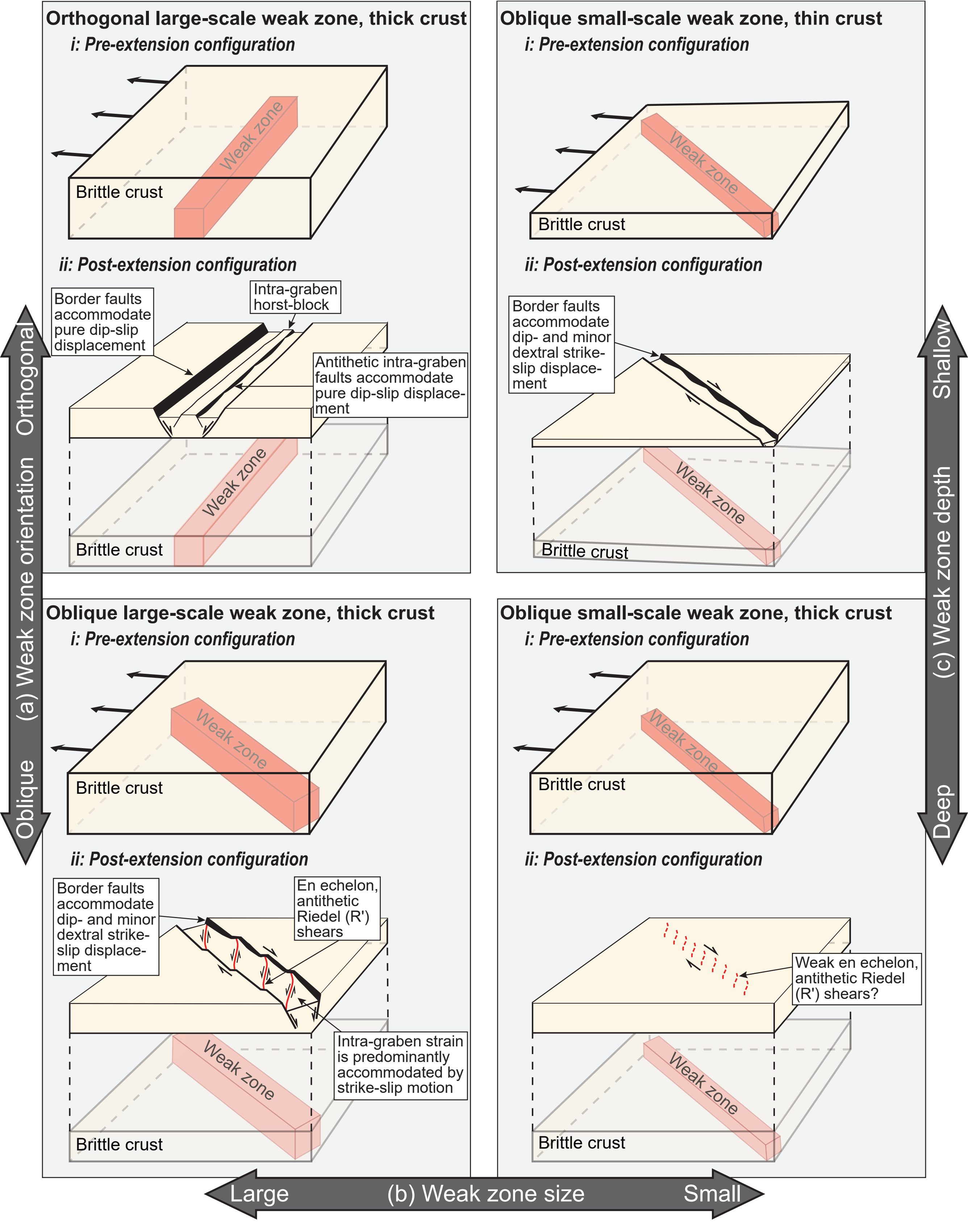

Figure 10: Schematic models highlighting the variability in the pattern of strain distribution and localization during rifting. (a) Left column shows variability in strain localization pattern controlled by the orientation of pre-existing weak zones with respect to the extension direction (i.e. orthogonal vs. oblique system), (b) Lower row shows variability in strain localization pattern controlled by the size of pre-existing weak zones, that is, large-scale weak zones exert significant control on the cover faulting pattern, whereas small-scale weak zones exert limited influence, (c) Right column shows variability in strain localization pattern controlled by the thickness of the overburden brittle layer or depth of pre-existing weak zones (not drawn to scale).